AFRL-AFOSR-VA-TR-2024-0222

Peptide-driven Exfoliation and Organization of Multi-compositional 2D Nanomaterials

Knecht, Marc
UNIVERSITY OF MIAMI
1320 SOUTH DIXIE HIGHWAY STE 650
CORAL GABLES, FL, 33146
USA

05/14/2024
Final Technical Report

Air Force Research Laboratory
Air Force Office of Scientific Research
Arlington, Virginia 22203
Air Force Materiel Command

REPORT DOCUMENTATION PAGE

PLEASE DO NOT RETURN YOUR FORM TO THE ABOVE ORGANIZATION.

1. REPORT DATE	2. REPORT TYPE	3. DATES COVERED	
20240514	Final	START DATE 20180801	END DATE 20220731

4. TITLE AND SUBTITLE
Peptide-driven Exfoliation and Organization of Multi-compositional 2D Nanomaterials

5a. CONTRACT NUMBER	5b. GRANT NUMBER	5c. PROGRAM ELEMENT NUMBER
	FA9550-18-1-0329	61102F
5d. PROJECT NUMBER	**5e. TASK NUMBER**	**5f. WORK UNIT NUMBER**

6. AUTHOR(S)
Marc Knecht

7. PERFORMING ORGANIZATION NAME(S) AND ADDRESS(ES)
UNIVERSITY OF MIAMI
1320 SOUTH DIXIE HIGHWAY STE 650
CORAL GABLES, FL 33146
USA

8. PERFORMING ORGANIZATION REPORT NUMBER

9. SPONSORING/MONITORING AGENCY NAME(S) AND ADDRESS(ES)	10. SPONSOR/MONITOR'S ACRONYM(S)	11. SPONSOR/MONITOR'S REPORT NUMBER(S)
Air Force Office of Scientific Research 875 N. Randolph St. Room 3112 Arlington, VA 22203	AFRL/AFOSR RTB2	AFRL-AFOSR-VA-TR-2024-0222

12. DISTRIBUTION/AVAILABILITY STATEMENT
A Distribution Unlimited: PB Public Release

13. SUPPLEMENTARY NOTES

14. ABSTRACT
This research program focuses on the use of biomimetic peptide-based approaches for the exfoliation and controlled assembly of two-dimension (2D) nanosheet heterostructures. Recent breakthroughs in elucidating the unique properties of 2D nanomaterials signify that these structures are poised to disrupt current electronic-based materials. To fundamentally understand and exploit these properties, nanosheet heterostructures must be created where the structure, composition, and relative orientation of the sheets can be precisely controlled. While conventional approaches cannot readily achieve such capabilities, we hypothesize that the precision of biological-materials recognition can be exploited to access such heterostructures, to allow for fundamental studies on the electronic and optical properties of 2D material heterostructures that cannot presently be accessed. For this, Biomolecular Exfoliant and Assembling Motifs (BEAMs) will be used to drive the exfoliation of bulk stacked materials
into individual nanosheets under ambient conditions. The BEAMs, which are composed of materials-specific peptides and fatty acids (Figure 1), will also be responsible for the dispersion and organization of multiple 2D nanosheets in water to generate heterostructures with control over the size and arrangement of the materials. This will generate a versatile platform for enabling fundamental studies on the basis of 2D nanosheet electronic properties. This platform would find immediate use for a variety of DoD relevant applications such as label free biomarker sensing via Field Effect Transistors (FETs) at unprecedented detection
limits, flexible and transparent optoelectronic devices, low density transistors, lasers and other optical devices, etc. Our biomimetic strategy for the generation of 2D nanosheet heterostructures is illustrated in Figure 1. To exfoliate the bulk layered material, a hybrid BEAM biomolecular construct is used. This construct is designed with three domains: two nanosheet-specific peptide binding domains placed at either end of the BEAM, with a central fatty acid domain. In this arrangement, the peptide with affinity for the bulk layered materials is envisioned to intercalate between the different layers of the structure, exposing both the fatty acid and second peptide domain to solution. With this orientation, significant stress will be placed upon the system, disrupting the non-covalent interactions that maintain the bulk sheet stacking, leading to exfoliation of the material to individual sheets. Since this process is anticipated to take place in water at low temperatures, minimal degradation of the individual sheets should occur. Once separated, secondary sheets of a disparate material can be added into the system, where formation of heterostructures is anticipated based upon the binding of the secondary materials binding domain of the BEAM. Based upon the regiospatial binding specificity of the two peptides (i.e. edge or basal plane), either vertical-stacking or lateral organization of the two different nanosheets is anticipated.

15. SUBJECT TERMS

16. SECURITY CLASSIFICATION OF:			17. LIMITATION OF ABSTRACT	18. NUMBER OF PAGES
a. REPORT	b. ABSTRACT	c. THIS PAGE		
U	U	U	UU	34

19a. NAME OF RESPONSIBLE PERSON	19b. PHONE NUMBER *(Include area code)*
BENNETT IBEY	000-0000

Standard Form 298 (Rev.5/2020)
Prescribed by ANSI Std. Z39.18

AFOSR Progress Report

Contract/Grant Title: Peptide-Driven Exfoliation and Organization of Multi-Compositional 2D Nanomaterials

Contract/Grant#: FA9550-18-1-0329

Reporting Period: 01 August 2021 – 31 July 2022

Technical Contact: Marc R. Knecht
Department of Chemistry
University at Miami
1301 Memorial Drive
Coral Gables, FL 33146
Phone: (305) 284-9351
Email: knecht@miami.edu

Co-Investigator:

Name	*Affiliation*	*Expertise*
Tiffany R. Walsh	Deakin University	Molecular simulations

A. Executive Summary

This research program focuses on the use of biomimetic peptide-based approaches for the exfoliation and controlled assembly of two-dimension (2D) nanosheet heterostructures. Recent breakthroughs in elucidating the unique properties of 2D nanomaterials signify that these structures are poised to disrupt current electronic-based materials. ***To fundamentally understand and exploit these properties, nanosheet heterostructures must be created where the structure, composition, and relative orientation of the sheets can be precisely controlled. While conventional approaches cannot readily achieve such capabilities, we hypothesize that the precision of biological-materials recognition can be exploited to access such heterostructures, to allow for fundamental studies on the electronic and optical properties of 2D material heterostructures that cannot presently be accessed***. For this, Biomolecular Exfoliant and Assembling Motifs (BEAMs) will be used to drive the exfoliation of bulk stacked materials into individual nanosheets under ambient conditions. The BEAMs, which are composed of materials-specific peptides and fatty acids (Figure 1), will also be responsible for the dispersion and organization of multiple 2D nanosheets in water to generate heterostructures with control over the size and arrangement of the materials. This will generate a versatile platform for enabling fundamental studies on the basis of 2D nanosheet electronic properties. This platform would find immediate use for a variety of DoD relevant applications such as label free biomarker sensing via Field Effect Transistors (FETs) at unprecedented detection limits, flexible and transparent optoelectronic devices, low density transistors, lasers and other optical devices, *etc*.

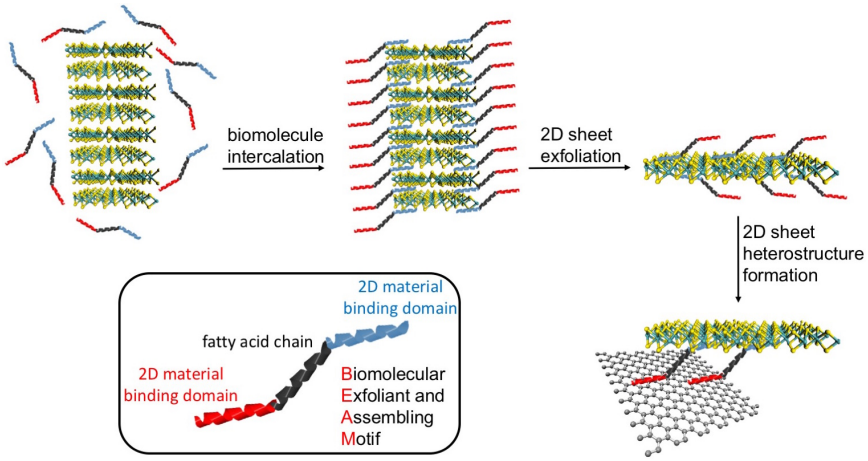

Figure 1. Biomolecular-driven exfoliation and controlled assembly of 2D nanomaterials. For this, Biomolecular Exfoliant and Assembling Motifs (BEAMs) will be used that combine two disparate 2D-material binding domains spaced by a fatty acid. These biomolecules are anticipated to exfoliate bulk layered materials and drive nanosheet heterostructure formation *in situ* via binding of the biological domains.

Our biomimetic strategy for the generation of 2D nanosheet heterostructures is illustrated in Figure 1. To exfoliate the bulk layered material, a hybrid BEAM biomolecular construct is used. This construct is designed with three domains: two nanosheet-specific peptide binding domains placed at either end of the BEAM, with a central fatty acid domain. In this arrangement, the peptide with affinity for the bulk layered materials is envisioned to intercalate between the different layers of the structure, exposing both the fatty acid and second peptide domain to solution. With this orientation, significant stress will be placed upon the system, disrupting the non-covalent interactions that maintain the bulk sheet stacking, leading to exfoliation of the material to individual sheets. Since this process is anticipated to take place in water at low temperatures, minimal degradation of the individual sheets should occur. Once separated, secondary sheets of a disparate material can be added into the system, where formation of heterostructures is anticipated based upon the binding of the secondary materials binding domain of the BEAM. Based upon the

regiospatial binding specificity of the two peptides (*i.e.* edge or basal plane), either vertical-stacking or lateral organization of the two different nanosheets is anticipated. Once these structures are generated, characterization of the emergent electronic properties will be processed where heterostructures composed of up to three different exemplar 2D nanosheet compositions will be probed: graphene as a conductor, *h*-BN as an insulator, and MoS_2 as a semiconductor. Graphene and *h*-BN have similar lattices, while MoS_2 is quite different with a sandwich MX_2 lattice (Mo atom plane with S atoms above and below). Our research goals will be advanced through completion of the following tasks that closely integrate complementary experimental (***Knecht***) and computational (***Walsh***) approaches:

Task 1. Peptide-driven exfoliation for the isolation of individual 2D nanosheets from bulk layered materials.

Task 2. Stacked 2D nanosheet heterostructure generation via basal plane binding peptides.

Task 3. Increased heterostructure complexity via bio-based lateral 2D nanosheet organization.

Summary of the Past 12 Months:
We have made substantial progress on the project during our final year of funding, 2022. A brief summary of each advance is included immediately below where an expanded discussion is included in Section B for each topic.

B1. Achieving Regioselective Materials Binding on Graphene and *h*-BN using Multidomain Peptides (BEAMs): In this work, a BEAM molecule was synthesized, comprising a graphene-binding peptide P1 at the N-terminal end, a *h*-BN binding peptide at the C-terminal end, linked by a 10-carbon fatty acid, F_{10}, denoted P1C-F_{10}F-CBP7. Quartz crystal microbalance measurements enabled quantification of the binding free energy of this BEAM on both graphene and *h*-BN surfaces. The biomolecular overlayer on *h*-BN featured substantial viscoelasticity compared with graphene, which is attributed to the greater entropic contribution to adsorption on this surface. Advanced sampling molecular simulations indicated that the two peptide domains preferentially bound their respective target surfaces, and also highlighted a clear lack of inter-domain interaction.

B2. Graphene Exfoliation using Multidomain Peptides (BEAM): This work demonstrated that the newly proposed hybrid molecule, BEAM, was able to bind the solvent-exposed graphene surface in a similar manner to the P1 peptide or the fatty acid conjugated molecule P1CF_{10} to both enable the exfoliation of the graphene sheets under sonication conditions and stabilize the resultant colloidal suspension of the graphene sheets in water. This suggests that incorporation of additional functionality (*e.g.*, the BP7 peptide) into the biomolecular construct does not interfere with graphene exfoliation. The results further suggest a stronger interaction between the P1 domain of the BEAM with the graphene surface, as anticipated from the original target affinity of the peptide. This indicates that the BP7 domain may remain available for *h*-BN binding for eventual heterostructure formation.

B3. Variation of BEAM Sequence and Effects on Binding and Exfoliation: This work explored the effects of the order of the peptide within the bifunctionals on the binding affinity to the graphene surface and the exfoliation of graphene nanosheets from bulk graphite. The order of the peptides had a slight impact on the binding affinity, showing a diminished affinity for graphene when the BP7 is attached on the N-terminus while the affinity increased when the P1 peptide was attached to the N-terminus. Additionally, each bifunctional molecule was shown to have the ability to exfoliate graphene regardless of the peptide order, as supported by evidence from molecular

dynamics simulations. The size and height of the sheets were not affected and all bifunctionals appeared to produce identical quantity of graphene sheets with similar quality.

B4. Sustainable, Aqueous Exfoliation of MoS_2 via Bio-inspired Avenues: MoS_2 materials were exfoliated in aqueous media with the support of a MoS_2-binding peptide and sonication. Both capped CMoSBP1 and uncapped MoSBP1 peptides were demonstrated to facilitate the exfoliation process, in which uncapped MoSBP1 peptides were found to be more efficient in exfoliating the MoS_2 into smaller structures. The exfoliated nanosheets were found to have different morphologies based upon the capped *vs*. uncapped structure of the peptide, which likely arises from the interactions between the material and biomolecule. Molecular simulations of both the initial exfoliation process and the stability of the resultant exfoliated sheets in solution were both consistent with the experimental data. Furthermore, the experimentally-observed differences in the exfoliated product for the capped and uncapped systems can in part be explained by the calculated free energy profiles related to the reunification of peptide-decorated MoS_2 nanosheets. The lesser protection conferred by the capped peptides is likely due to the fact that the sheets decorated by capped peptides can approach relatively closer compared with their uncapped counterparts.

External Collaborations: In the final year of the grant, we have maintained collaborations with the Wilson and Costantini groups at the University of Warwick, U.K. on microscopy of molecular adlayers on graphene. We have also continued our long-standing collaboration with Rajesh Naik at AFRL, which resulted in multiple joint publications with the Naik team. Finally, we have worked with Dr. Peter Frazier at Cornell University and Dr. Mark Swihart at SUNY Buffalo on using machine learning approaches for the design of materials-selective peptides.

Publications:

1. Pham, L. N.; Perdomo, Y.; Walsh, T.R.; Knecht, M.R. Sustainable, Aqueous Exfoliation of MoS_2 via Bioinspired Avenues, in preparation.
2. Jin, R.; Brljak, N.; Slocik, J.; Rao, R.; Knecht, M.R.; Walsh, T.R. Graphene exfoliation using multidomain peptides, *J. Mater. Chem. B* **2024**, in press.
3. Brooks, S.C.; Jin, R.; Zerbach, V.C.; Zhang, Y.; Walsh, T.R.; Rosi, N.L. Single Amino Acid Modifications for Controlling the Helicity of Peptide-Based Chiral Gold Nanoparticle Superstructures, *J. Am. Chem. Soc.* **2023**, *145*, 6546-6553.
4. Jin, R.; Brljak, N.; Sangrigoli, R.; Walsh, T.R.; Knecht, M.R. Achieving Regioselective Materials Binding using Multidomain Peptides*, Nanoscale* **2022**, 14, 14113-14121.
5. Perdomo, Y.; Jin, R.; Parab, A.D.; Knecht, M.R.; Walsh, T.R. Manipulation of Peptide-Fatty Acid Bioconjugates on Graphene: Effects of Fatty Acid Chain Length and Attachment Point, *J. Mater. Chem. B* **2022**, *10*, 6018-6025.
6. Pham, N. L.; Walsh, T.R. Predicting Biomolecule Adsorption on MoS_2 Nanosheets with High Structural Fidelity, *Chem. Sci.* **2022***, 13*, 5186 – 5195. *(Pick of the Week)*
7. Jin, R.; Walsh T.R. Modeling-Led Materials-Binding Peptide Design for Hexagonal Boron Nitride Interfaces, *Adv. Mater. Interfaces,* **2022**, *9*, 2102397.
8. Pham, N. L.; Walsh, T.R. Design Traits for Diblock Copolymer Coating Properties on $NaGdF_4$ Upconversion Nanoparticles, *ACS Appl. Polym. Mater.* **2022**, *4,* 5224-5233.
9. Marsden, A. J.; Skilbeck, M.; Healey, M.; Thomas, H. R.; Walker, M.; Edwards, R. S.; Garcia, N. A.; Vuković, F.; Jabraoui, H.; Walsh, T. R.; Rourke, J. P.; Wilson, N. R. From Graphene to Graphene Oxide: the Importance of Extended Topological Defects, *Phys. Chem. Chem. Phys.* **2022**, *24*, 2318-2331.

10. Jin, R.; Vuković, F.; Walsh T. R. Peptide-Driven Exfoliation and Dispersion Mechanisms of Graphene in Aqueous Media, *J. Phys. Chem. Lett.* **2021**, *12*, 11945-11950.
11. Hughes, Z. E.; Nguyen, M. A.; Wang, J.; Liu, Y.; Swihart, M. T.; Poloczek, M.; Frazier, P. I.; Knecht, M. R.; Walsh, T. R.; Tuning Materials-Binding Peptide Sequences towards Gold- and Silver-Binding Selectivity with Bayesian Optimization, *ACS Nano* **2021**, *15*, 18260-18269.
12. Awuah, J. B.; Walsh T. R. Sequence control over emergent nano-patterns in dipeptide adlayers at the graphene interface, *Appl. Surf. Sci*. **2021**, *560*, 149605.
13. Brljak, N.; Knecht, M.R.; Walsh, T.R. Controlling the Orientation and Viscoelasticity of Materials-Binding Peptides on Hexagonal Boron Nitride Using Fatty Acids, *J. Phys. Chem. B* **2021**, *125*, 10621-10628.
14. Brljak, N.; Jin, R.; Walsh, T.R.; Knecht, M.R. Selective Manipulation of Peptide Orientation on Hexagonal Boron Nitride Nanosheets, *Nanoscale* **2021**, 12, 5670-5678.
15. Pham, L.N.; Walsh, T.R. Force Fields for Water-Surface Interaction: Is Reproduction of the Experimental Water Contact Angle Enough?, *Chem. Commun.* **2021**, *57*, 3355-3358.
16. Parab, A.D. Dureja, R.; Rao, R.; Slocik, J.M.; Naik, R.R.; Walsh, T.R.; Knecht, M.R. Identification of Parameters Controlling Peptide-Driven Graphene Exfoliation in Aqueous Media, *Langmuir* **2021**, *37*, 1152-1163.
17. Parab, A.D.; Budi, A.; Brljak, N.; Knecht, M.R.; Walsh, T.R. Modulation of Peptide-Graphene Interfaces via Fatty Acid Conjugation, *Adv. Mater. Interfaces* **2021**, *8*, 2001659.
18. Brljak, N.; Parab, A.D.; Rao, R.; Slocik J.M., Naik, R.R.; Knecht, M.R.; Walsh, T.R. Material Composition and Peptide Sequence Affects Biomolecule Affinity to and Selectivity for *h*-Boron Nitride and Graphene, *Chem. Commun.* **2020**, *56*, 8834-8837.
19. Parab, A.D.; Budi, A.; Slocik, J.M.; Rao, R.; Naik, R.R.; Walsh, T.R.; Knecht, M.R. Molecular-Level Insights on Biologically-Driven Graphite Exfoliation for the Generation of Graphene in Aqueous Media, *J. Phys. Chem. C* **2020**, *124*, 2219-2228.
20. Awuah, J.B.; Walsh, T.R. Side-Chain Effects on the Co-Existence of Emergent Nanopatterns in Amino Acid Adlayers on Graphene. *Nanoscale* **2020**, *12*, 13662-13673.
21. Awuah, J.B.; Walsh, T.R. Predictions of Pattern Formation in Amino Acid Adlayers at the *In Vacuo* Graphene Interface: Influence of the Termination State. *Small* **2020**, *16*, 1903403.
22. Walsh, T.R.; Knecht, M.R. Biomolecular Materials Recognition in Two Dimensions: Peptide Binding to Graphene, *h*-BN, and MoS_2 Nanosheets as Unique Bioconjugates, *Bioconj. Chem.* **2019**, *30*, 2727-2750.
23. Budi, A.; Walsh, T.R. A Bespoke Force Field to Describe Biomolecule Adsorption at the Aqueous Boron Nitride Interface. *Langmuir* **2019**, *35*, 16234-16243.
24. Bell, E.C.; Munro, C.J.; Shukla, D.; Cohn, J.L. Knecht, M.R. Biomimetic Strategies to Produce Catalytically Reactive CuS Nanodisks, *Nanoscale Adv.* **2019**, *1*, 2857-2865. (Featured on the cover of the August 2019 issue.)
25. Parab, A.; Slocik, J.M.; Naik, R.R.; Knecht, M.R. Peptide-Driven Fabrication of Catalytically Reactive Rhodium Nanoplates, *ACS Appl. Nano Mater.* **2018**, *1*, 7149-7158.

Changes in Research Objectives, If any: None

Changes in AFOSR program manager, if any: None

Extensions granted or milestones slipped, if any: None

Include any new discoveries, inventions, or patent disclosures during this period (if none, report none): None

B. Progress Toward Year 3 Goals

B1. Achieving Regioselective Materials Binding on Graphene and *h*-BN using Multidomain Peptides (BEAMs).

Here, we demonstrate the production of a bio-based bifunctional ligand with regiospecific binding to two different nanosheet compositions: graphene and *h*-BN. This construct, termed a Biomolecular Exfoliant and Assembling Motif (BEAM), positions the P1 and BP7 peptides in sequence, separated by a fatty acid spacer of 10 carbons in length, as shown in Scheme B1.1. Once prepared, the affinity of the BEAM molecule on both graphene and *h*-BN was quantified using quartz crystal microbalance (QCM) analysis, which demonstrated compositionally dependent binding affinity and viscoelasticity of the bio-overlayer generated. This overlayer was subsequently imaged on graphene using atomic force microscopy (AFM). To complement these experimental data, advanced sampling molecular dynamics (MD) simulations were used to predict the most likely conformations for the BEAM adsorbed at the aqueous graphene and *h*-BN interfaces. These simulations indicate that the BEAM design can meet two key criteria for realizing regioselective ligand binding of target materials, namely the binding specificity of each materials-binding domain in the BEAM for its target material, together with the ability to maintain spatial separation of the two materials-binding domains to limit the degree of detrimental inter-domain interactions. These experimental and computational results, in concert, are key to demonstrate the ability of a single molecule to regiospecifically bind to two different material compositions. Such capabilities could prove to be important for the future production of complex materials required for a variety of applications ranging from energy harvesting/storage to biomedical systems.

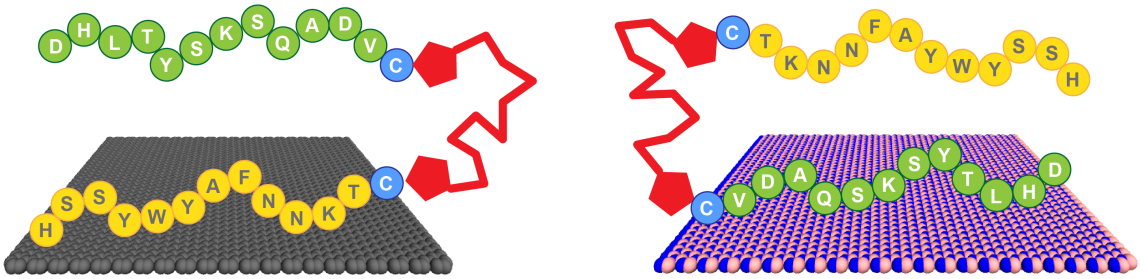

Scheme B1.1 Regiospecific binding of the BEAM molecule onto graphene, via the P1 domain (left), and *h*-BN, via the BP7 domain (right).

To generate the bifunctional BEAM molecule, a facile synthetic process was developed (Figure B1.1), which can be generalized to incorporate different materials binding peptides. The synthesis began with production of the $F_{10}F$ fatty acid domain by replacing the two terminal chlorides present in sebeacoyl chloride with two maleimide groups. This would allow for bio-orthogonal coupling of the peptides via thiol maleimide coupling of the sequences at the fatty acid linker. Coupling of each peptide binding domain was done sequentially where the first peptide (CBP7) was mixed with the $F_{10}F$, which was present in excess to limit double peptide coupling to a single fatty acid. Once the first coupling was complete, the second peptide (P1C) was added to the system to couple and generate the final construct. After each peptide coupling step, the materials were purified by HPLC and

confirmed via MALDI-TOF mass spectrometry. Using this approach, a final molecule with a global structure of P1C-F_{10}F-CBP7 was prepared, which is referred to as the BEAM.

Once the BEAM molecule was synthesized, the binding affinity to both graphene and *h*-BN were studied by using QCM. This highly sensitive technique can measure small changes of mass adsorbed at a surface and can be used to determine the binding affinity of biomolecules onto a target material. Using standard methods, Au QCM sensors were coated with a single layer of either graphene or *h*-BN. During the binding measurements, aqueous solutions of the BEAM were flowed over the two different sensors ranging in concentration from 5.0 - 17.5 μg mL^{-1}. The frequency change over time was measured where the inverted plot for BEAM binding at both graphene and *h*-BN are shown in Figure B1.2a and b, respectively. As anticipated, clear changes in binding are evident as a function of BEAM concentration and the underlying sensor composition. Fitting of each binding surface can then be processed using the Langmuir isotherm, from which k_{obs} values can be obtained. These k_{obs} values can then be plotted as a function of BEAM concentration (Figure B1.2c and d), from which a variety of kinetic parameters of binding can be determined via the line of best fit (*e.g.*, slope = k_a and *y*-intercept = k_d). Using the k_a and k_d values, K_{eq} can be determined and subsequently used to calculate the free energy of BEAM binding (ΔG) to both the graphene and *h*-BN surfaces.

From the QCM binding analysis, a free energy of binding for the BEAM on graphene was determined to be -35.3 ± 1.9 kJ mol^{-1}; however, when the same binding analysis was processed on *h*-BN, the ΔG value was calculated as -38.4 ± 1.2 kJ mol^{-1}, as shown in Table B1.1. Based upon these values, this indicates that the BEAM molecule binds stronger to *h*-BN over graphene.

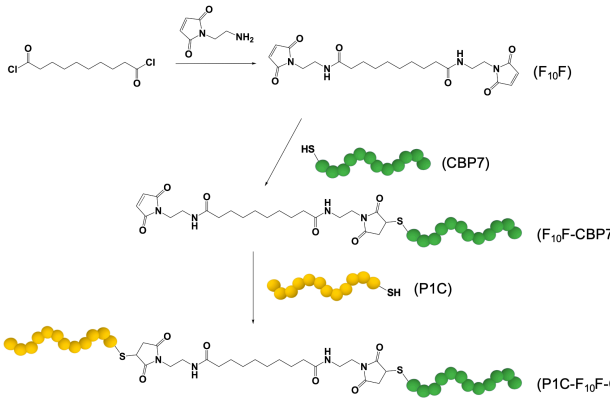

Fig. B1.1 Synthesis of the BEAM molecule. The $F_{10}F$ fatty acid domain is prepared first, followed by the attachment of CBP7 and then by P1C in a second coupling

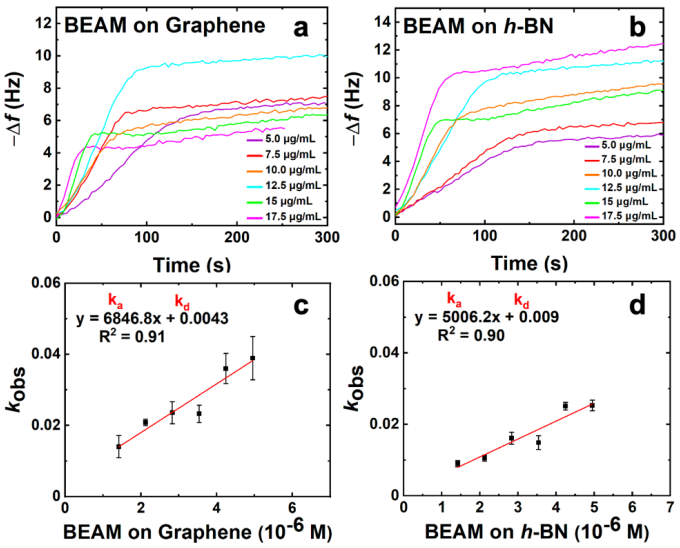

Fig. B1.2 QCM analysis of the binding affinity of the BEAM molecule. Parts (a) and (b) show the inverted frequency change over time for a range of concentrations for BEAM binding to graphene and *h*-BN, respectively. Parts (c) and (d) present the linear relationship between k_{obs} and BEAM concentration for (c) graphene and (d) *h*-BN.

Table B1.1 Free energy of binding and maximum dissipation energy of the BEAM and parent peptides adsorbed on graphene and *h*-BN.

	h-BN		Graphene	
Peptide	ΔG (kJ mol^{-1})	Maximum dissipation energy (u)	ΔG (kJ mol^{-1})	Maximum dissipation energy (u)
P1CF_{10}FCBP7	-38.4 ± 1.2	1.88	-35.3 ± 1.9	0.72
P1	-33.0 ± 2.2	0.14	-35.6 ± 2.3	0.20
BP7	-29.5 ± 0.3	0.11	-33.5 ± 3.9	0.27
BP7CF_{10}	-30.2 ± 2.6	1.81	-	-
F_{10}CBP7	-33.3 ± 1.6	0.36	-	-

Such results were quite surprising as this is different than what was previously reported for the parent peptides, BP7 and P1, both of which demonstrated greater affinity for graphene over *h*-BN (Table B1.1). Furthermore, these values also indicated that the BEAM bound either equivalently or stronger to both nanosheet surfaces as compared to the individual peptides, based upon the magnitude of the ΔG values. This suggests that changes in the biomolecular structure could be important in controlling the absolute affinity of the ligand to the material surface.

It is important to note that while the difference in the ΔG values is somewhat small, prior studies have indicated that such differences can lead to significant variations in the coverage of the peptide on the target surface. In this prior work focused on comparing the fractional surface coverage (θ) of two peptides on the same surface (*e.g.* simultaneous binding of P1 and BP7 on graphene), the ratio of the equilibrium constants of binding for the two peptides is equivalent to the surface coverage ratio (*e.g.* θ_{P1}/θ_{BP7}) when the solution concentration of the two peptides is equal. Using the K values obtained previously for P1 and BP7 binding to graphene and *h*-BN, 2.4 and 4.1 times more P1 would be bound to graphene and *h*-BN, respectively, compared to the BP7 peptide. While a similar calculation cannot be performed using the BEAM (*e.g.* one peptide binding two different surfaces), this demonstrates that a significant degree of surface selectivity can be achieved based upon relatively small differences in ΔG values.

In addition to the frequency change, the dissipation energy was also monitored during the QCM study, which provided direct insight into the viscoelasticity of the BEAM overlayer generated at the nanosheet surface. Figure B1.3 shows the dissipation energy over time as the BEAM molecule adsorbs to the graphene and *h*-BN surfaces. It is evident that as the BEAM molecule binds, the dissipation energy increases for all concentrations, suggesting varying degrees of viscoelasticity as a function of biomolecule concentration. The maximum dissipation energy measured for BEAM binding to graphene and *h*-BN is summarized in Table B1.1, revealing greater viscoelasticity for the BEAM bound to *h*-BN as compared to graphene.

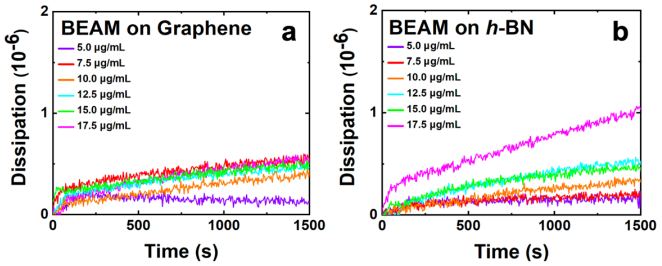

Fig. B1.3 Dissipation energy analysis of the BEAM binding to (a) graphene and (b) *h*-BN.

Such effects were somewhat surprising as the results presented suggested that a viscoelastic layer was generated on graphene. Previous studies of peptide overlayer formation on graphene demonstrated notably lower dissipation energy, indicating that a rigid monolayer structure was generated; however, when peptides modified with fatty acids are adsorbed to *h*-BN, significant viscoelasticity has been noted. The main difference likely arises due to the size of the biomolecule, where the BEAM is more than double the size of the individual P1 and BP7 peptides, and the multiple different binding domains present in the BEAM molecule. These two effects are likely to drive the emergence of a more viscoelastic interface, potentially through the formation of extended molecular structures away from the nanosheet surface. It is noted that these dissipation energy values are relatively high for binding at nanosheet surfaces, especially for the BEAM bound to *h*-BN, indicating that a highly viscoelastic interface was prepared on *h*-BN material.

Additionally, AFM was used to image the overlayer structure of the BEAM molecule on the graphene surface. For this, highly oriented pyrolytic graphite (HOPG) was employed as the graphene surface for peptide overlayer formation; previous work has shown that

peptide binding to HOPG is comparable to a single sheet of graphene. For the analysis, the BEAM solution was drop casted onto cleaved HOPG and allowed to sit for 15 min. Afterwards, the HOPG surface was rinsed with deionized water and dried prior to imaging in tapping mode. Figure B1.4 shows the morphology of the BEAM peptide overlayer on HOPG, which demonstrated high coverage of the biomolecule on HOPG. Within the overlayer structure, small pores of various sizes and morphologies were noted. Such a porous morphology is consistent with overlayers of P1, both with and without fatty acids incorporated; however, the BEAM-based overlayer has considerably fewer pores that were generally smaller. The depth of pores was determined and used to calculate the height of the peptide overlayer, which was ~3.5 nm. This thickness was notably greater than those of the P1-based peptides; however, such an increase in thickness was anticipated based upon the larger size of the BEAM.

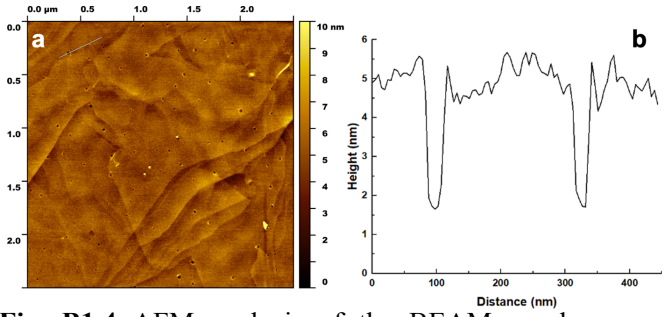

Fig. B1.4 AFM analysis of the BEAM overlayer on HOPG at a concentration of 0.5 mg mL^{-1}. Part (a) shows an area scan of the surface, while part (b) presents the height profile corresponding to the area indicated in the upper left section of part (a).

In addition to the experimental analysis, computational studies were also conducted. Advanced sampling simulations using REST-MD simulations were used to predict the likely ensemble of adsorbed conformations of the BEAM molecule adsorbed at the aqueous interfaces of both graphene and *h*-BN. The amount of residue-surface contact was determined from the REST-MD simulations, summarized in Figure B1.5. It is noted that a comparison of the absolute contact percentages across the two surfaces is not meaningful, given the differences in the two force-fields. On graphene, the P1 domain of the BEAM shows strong surface contact throughout most of the sequence, with a significant focus on the N-terminal half. The hydrophobic $F_{10}F$ linker also supported strong and consistent contact throughout, whereas the BP7 domain contact also supported a reasonably balanced distribution of contact sites along the length of the sequence. Comparison with data previously reported for the P1 and BP7 parent sequences indicated a spatial redistribution of the BEAM domain contact sites to the extremes of the BEAM ends (*i.e.*, the N-terminus of the P1 domain and the C-terminus of the BP7 domain). On *h*-BN, the effects of the conjugation into the BEAM revealed an overall loss of contact for the P1 domain compared with the P1 parent, whereas for the BP7 domain, the degree of this change was less clear cut.

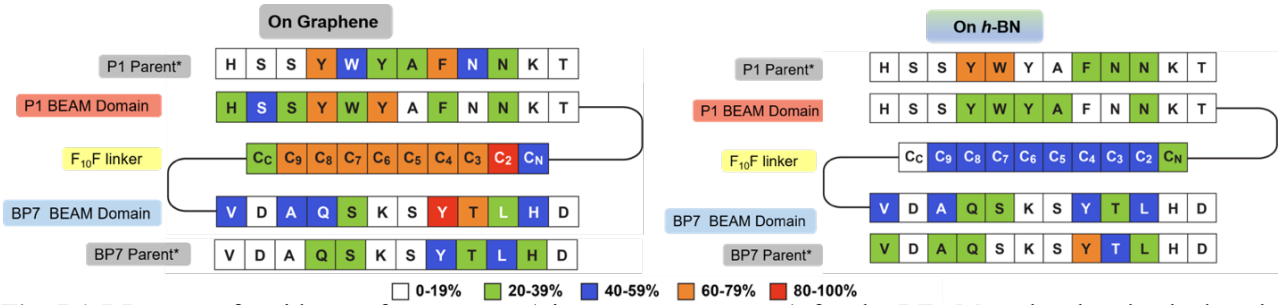

Fig. B1.5 Degree of residue-surface contact (given as a percentage) for the BEAM molecule adsorbed at the aqueous graphene and *h*-BN interfaces. *Corresponding data for the P1 and BP7 parent peptides taken from previous work.

However, not all residues bind with equal strength, meaning that the contact patterns alone do not capture the binding in its entirety. Using an enthalpic binding score, as defined in previous work, which combines both the amino acid binding free energies on the two surfaces and the degree of contact, the binding specificity of each domain in the BEAM molecule can be estimated. For graphene, the P1 BEAM domain had a calculated binding score of -62.3 kJ mol^{-1} compared with a score of -58.9 kJ mol^{-1} for the BP7 BEAM domain, indicating materials specificity (*i.e.*, P1 domain binding was preferred over BP7 domain binding on graphene). Similarly, the binding scores on *h*-BN for the BP7 and P1 BEAM domains were -20.7 and -15.6 kJ mol^{-1}, respectively, indicating binding specificity of the BP7 domain over the P1 domain on its target *h*-BN surface. Again, direct comparison of the absolute values of these scores across the two materials is not meaningful due to the differences in the force-fields. Taken together, this enthalpic score analysis suggests that the two domains preferentially bind their anticipated target materials, achieving regioselective materials binding from the BEAM construct.

The entropic contributions to the overall binding can also be estimated, based on a clustering analysis, in which all frames in the REST-MD trajectory are grouped according to similarity in backbone structure (in which each group is a 'cluster'). This analysis can be used to calculate the discrete entropy of the cluster distribution (number of clusters and their relative populations), denoted here as S_{conf}. S_{conf} is a dimensionless quantity and is a measure of the number of thermally accessible structures in the adsorbed state. It is calculated to be 3.2 and 3.8 for the BEAM adsorbed at the aqueous graphene and *h*-BN interfaces, respectively. The greater entropic contribution to binding for the BEAM on *h*-BN suggests an entropically-driven process, as compared to a more enthalpically-driven process for BEAM/graphene binding with a lower S_{conf}, which offers an explanation for the stronger binding free energy of the BEAM on *h*-BN versus graphene.

The proposed entropically-driven binding on *h*-BN, contrasted with the more enthalpically-driven binding on graphene, can be linked with the dissipation observations from the QCM-D experiments. Following previous studies, the dissipation energy (and thus the viscoelasticity of the adsorbed BEAM overlayer) is proposed to be associated with the number of upright states in the

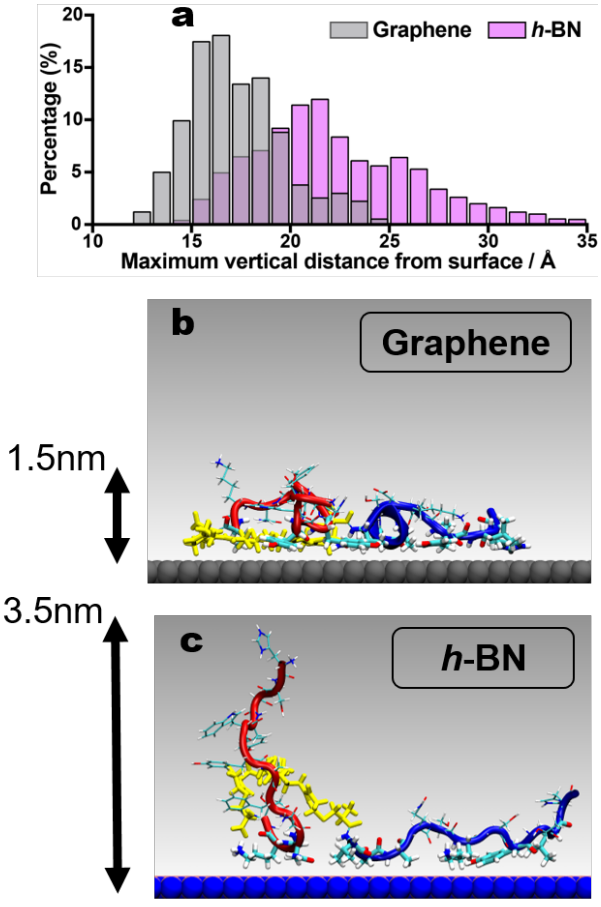

Fig. B1.6 (a) Histogram of the maximal vertical molecule-surface distance of the BEAM in the surface adsorbed state at the aqueous graphene and *h*-BN interfaces. Example snapshots of the BEAM molecule adsorbed on (b) graphene and (c) *h*-BN, with the maximal vertical molecule-surface distance indicated. Color scheme: P1 in red, $F_{10}F$ linker in yellow, BP7 in blue. Water not shown for clarity.

conformational ensemble, where regions of the BEAM molecule protrude away from the surface and into solution. Here, the BEAM adsorbed on *h*-BN supports a substantially enhanced population of upright states compared to the structures adsorbed to graphene, which can explain the relatively higher dissipation energy value observed for *h*-BN. To quantify this, the maximal value of the vertical molecule-surface distance was calculated over all frames in the two REST-MD trajectories, summarized in the histogram of Figure B1.6a. On *h*-BN, it is clear the BEAM adopts a greater fraction of surface-extended states, compared with the BEAM adsorbed to graphene. Example snapshots of the two trajectories provided in Figure B1.6b and c reveal the more prone, horizontal contact mode on graphene compared with the upright state shown for the *h*-BN bound BEAM ligand.

Another critical measure of success for these bioconjugate molecules to achieve regiospecific binding is the ability to keep the two materials-binding domains separate, such that their availability for binding to the target surfaces is maximized. This shifts the focus from the molecule-surface interactions to the intra-molecule interactions, which were quantified as summarized in Figure B1.7 for the aqueous graphene interface. Figure B1.7a shows that each residue in the P1 domain and BP7 domain feature little interaction with the rest of the molecule overall, for the case of adsorption on graphene. The proportion of intra-molecule interactions is notably higher in the $F_{10}F$ linker region, which can in part be explained by the flexible nature of this alkane chain and its spatially compact methylene groups that allows for close methylene-methylene contact. These contact data presented in Figure B1.7a were broken down into three contributions for each residue in Figure B1.7b (analogous data shown in Figure B1.7c for adsorption at the aqueous *h*-BN interface); intra-BEAM interactions with the P1 domain, with $F_{10}F$, and with the BP7 domain. These clearly show that residues in the P1 domain chiefly interact either with residues in the P1 domain or in the linker domain, whereas the opposite is true for the residues in the BP7 domain. This limitation in the degree of inter-domain cross-talk when adsorbed at both materials interfaces indicate that the two materials-binding domains can remain spatially separated in the surface-adsorbed state to achieve

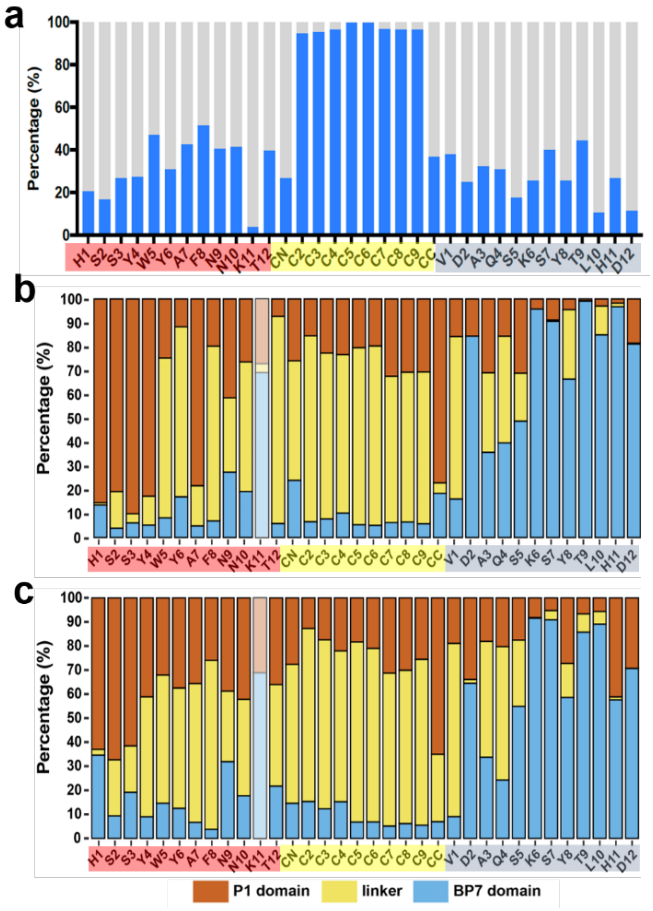

Fig. B1.7 Summary of intra-BEAM interactions in the surface-adsorbed state at the aqueous interfaces. (a) The proportion of the trajectory for which a given residue has any interaction with the rest of the BEAM molecule, indicated by blue bars, on the graphene surface. The residues indicated on the ordinate are colored by domain (red for the P1 domain, yellow for $F_{10}F$, blue for the BP7 domain). (b) Breakdown of each blue bar in panel a) into interactions with the P1 domain (red bars), $F_{10}F$ (yellow bars) and BP7 domain (blue bars). Data for K11 are greyed out due to extremely low data volume. (c) Similar breakdown for BEAM adsorption at the *h*-BN interface.

regiospecific binding of the BEAM molecule to the target materials.

Finally, as a prelude to future investigations, MD simulations were used to explore the capability of the BEAM molecule to maintain a structurally-stable hetereostacked bilayer of a graphene nanosheet and an *h*-BN nanosheet in liquid water. In these simulations, a graphene nanosheet and an *h*-BN nanosheet, both of 7.2-7.5 nm diameter, were placed in a vertically stacked configuration, with a vertical gap of ~ 1.5 nm. Five BEAM molecules were placed in this gap, and the cubic periodic cell (~13 nm dimension) was filled with liquid water and subjected to MD simulation in the *NVT* ensemble at room temperature. The BEAM molecule was found to promote the stability of this heterostack arrangement. Stable configurations were found to remain so over 50 ns of production simulation; an example of a final configuration is provided in Figure B1.8.

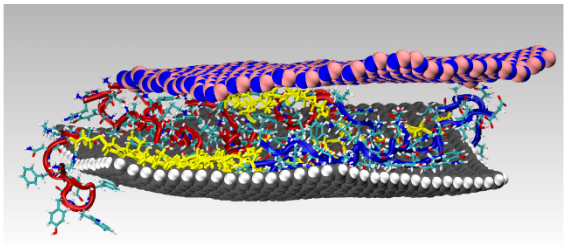

Fig. B1.8 Snapshot shown in side view of an example heterostack of graphene and *h*-BN nanosheets (~7.5 nm in diameter), stabilized by BEAM molecules in liquid water. Water molecules

Based upon the differences in the ΔG values and the calculations of fractional surface coverage discussed above, a sequential approach to driving nanosheet assembly is proposed. In this situation, equivalent P1 and BP7 solution concentrations are present using the BEAM molecule, which displays one of each sequence as a nanosheet binding domain. When the BEAM is exposed to graphene, binding is anticipated where regiospecific adsorption of the P1 domain should occur (2.4 times more than BP7), thus presenting the BP7 domain preferentially to solution. Inclusion of *h*-BN sheets to this solution will drive binding of the secondary material, leading to heterostack formation. This capability is supported by the results of simulations shown in Figure B1.8, confirming that the BEAM molecule can indeed facilitate heterostack assembly and stability.

In conclusion, properties of a bifunctional biomolecule, referred to as a Biomolecular Exfoliant and Assembling Motif (BEAM), designed to achieve regiospecific binding capabilities for 2D materials were demonstrated and rationalized using an integration of experimental and molecular simulation approaches. The BEAM featured a graphene-binding domain containing the P1 sequence and an *h*-BN binding domain presenting the BP7 sequence, separated by a fatty acid chain; it was demonstrated to bind to aqueous interfaces of both materials, with stronger binding indicated for *h*-BN. The biomolecular overlayer on *h*-BN featured substantial viscoelasticity compared with graphene, which is attributed to the greater entropic contribution to adsorption on this surface. Advanced sampling molecular simulations indicate that the two peptide domains preferentially bound their respective target surfaces, and also highlight a clear lack of inter-domain interaction. These results show that ligands require significant complexity to achieve regiospecific affinity for two disparate materials, where biomolecular specificity could be instrumental to achieve such capabilities.

B2. Graphene Exfoliation using Multidomain Peptides (BEAMs).

Here, we explored the use of the BEAM for driving graphene exfoliation under low temperature, aqueous conditions. Based on earlier work, all-atom molecular dynamics (MD) simulations can provide key insights into this exfoliation process. Here, MD simulations were used to explore graphene exfoliation and the colloidal suspension capabilities of the BEAMs, indicating that these chimeric molecules can successfully produce exfoliated graphene in aqueous media. To experimentally confirm this capability, a probe sonication-based method was exploited to generate graphene sheets in significantly shorter times (1 h) as compared to bath sonication methods (12 h). Once the materials were obtained, they were fully characterized via spectroscopic and electronic methods to confirm the structure of the graphene nanosheets.

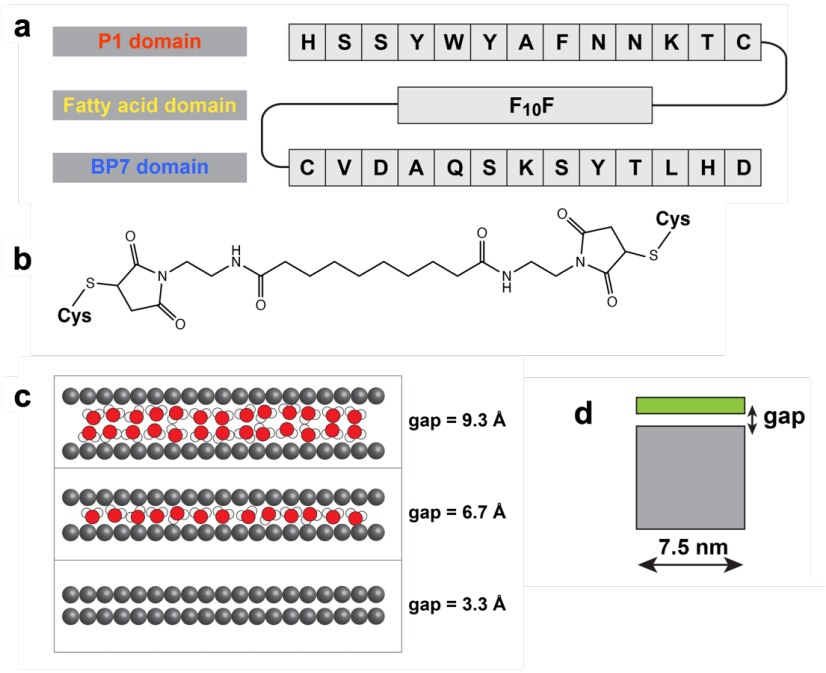

Fig. B2.1. BEAM molecule and the inter-sheet gap closure time of the gap in the absence of BEAM molecules. a) Chemical structure and sequence of the BEAM molecule. b) The 10-carbon fatty acid spacer linking the P1 domain and BP7 domain in the BEAM. c) The progress of the gap closure with different hydration states and corresponding (approximate) inter-sheet vertical spacings. d) Schematic indicating the expanded gap comprising a detached top-most sheet (green) from graphite stack (grey) for obtaining the gap closure time under sonication conditions in the absence of BEAM molecules.

The BEAM molecule (Figure B2.1a) was prepared with a P1 peptide domain at the N-terminus, a BP7 peptide domain at the C-terminus, and a 10-carbon-length fatty acid spacer (termed $F_{10}F$) positioned in between (such that the BEAM is denoted P1C-$F_{10}F$-CBP7). To connect each peptide domain to the centralized fatty-acid, a cysteine residue was introduced into the C-terminus of P1 and the N-terminus of BP7. This allowed for site specific coupling with two maleimide groups integrated at both ends of the $F_{10}F$ fatty acid (Figure B2.1b) using thiol maleimide coupling sequentially.

The success of the exfoliation process hinges on two stages: first, the sheets must be detached from the bulk material during sonication, and second, these detached sheets must be prevented from reunifying upon conclusion of the sonication process. Although experimental approaches can ultimately evaluate the success of exfoliation via observation

of the resultant colloidal suspension, it is challenging for experiment to directly verify the details of these two phenomena. In contrast, MD simulations can provide atomic-scale insights into each stage of the process. For the simulations, the parameters for describing the $F_{10}F$ domain were taken from previous work of modeling $F_{10}CP1$ and $P1CF_{10}$ (essentially P1 with the fatty acid at either termini). Comparing with the two parent peptides, this BEAM molecule exhibits stronger binding on the *h*-BN surface and similar binding free energy on the graphene surface. Moreover, replica exchange with solute tempering molecular dynamics (REST-MD) simulations indicated that the P1 domain of the BEAM interacted with the graphene surface strongly, as well as the $F_{10}F$ motif, and that the BP7 domain also maintained sufficient interactions with the surface using several anchor residues such as valine, alanine, glutamine, and tyrosine.

In this study, MD simulations were first used to examine the possibility and the mechanisms of dynamic insertion of the BEAM molecules into the expanded gap region between two graphene sheets, and the ability of the BEAM to maintain this gap, all done in the medium of liquid water. This process is representative of the first stage of graphene exfoliation from bulk graphite in aqueous media. As in our previous work, a model of a nine-layer graphite stack was prepared and the gap between the top two graphene sheets in the stack was expanded to 10 Å to mimic the expanded gap under sonication conditions, in the presence or absence of the BEAM in the NVT ensemble (Figure B2.1c). Only the very bottom graphene sheet was frozen in space and the rest of the sheets in the stack, including the top-most partially detached sheet, were completely free to move. Given that the BEAM molecule is longer than the P1 peptide or the $P1CF_{10}$ molecule examined in previous work, the size of the graphene sheet in the stack was also increased compared with previous studies, such that the graphene sheet diameter was ~7.5 nm (compared to a diameter of ~4.7 nm used previously).

The recombination timescale of the expanded gap, namely the possible reunification of the detached top graphene sheet with the graphite stack in the absence of the BEAM, was first estimated to obtain an average gap closure time. This establishes a baseline timescale against which the closure time in the presence of the BEAMs can be compared, enabling determination of the effectiveness of the BEAMs as exfoliating agents. Upon solvation of the BEAM-absent system, two layers of water molecules were initially observed in the expanded gap region. Four independent simulations in the absence of the BEAM molecules were run, and the average time for gap closure was 73.5 ns with the quickest gap closure time of 20.3 ns. For comparison, the corresponding gap-closure study using a smaller graphene sheet diameter (~4.7 nm diameter) yielded an averaged closure time of 91 ns in liquid water in the absence of peptide. The faster closure time reported here reflects the relatively greater surface area of the basal plane and the concomitant increase in overall van der Waals attraction between the two sheets relative to the smaller sheet dimensions used in our previous work. It is noted here that the absolute values of the closure times are not the key point of relevance, but rather provide a relative baseline against which the performance of the BEAMs can be evaluated. In the current study, the two water layers in the expanded gap first reduced to one layer, then diminished completely (Figure B2.1d), indicating closure.

Another two scenarios were then explored using MD simulations involving the BEAM molecules. This was done to explore two key stages of graphene exfoliation: the initial stage to probe the ability of the BEAM to intercalate into the expanded gap and maintain an open gap (*i.e.*, to prevent the top-most layer of graphite from re-uniting with the remainder of the stack), and the final stage probing the ability of the BEAM molecules to

decorate free (exfoliated) graphene sheets in solution and inhibit these exfoliated sheets from reuniting in water. In the first scenario, and following from previous studies, two different initial conditions were investigated, herein termed 'pre-insertion' and 'spontaneous insertion'. For the pre-insertion case, BEAM molecules were initially placed inside the expanded gap, and simulations were conducted to test the stability of the expanded gap in this 'pre-inserted' state (that is, the stability of the expanded gap was examined on the assumption that BEAM molecules could insert themselves into the expanded gap). The pre-insertion of the BEAMs was accomplished in two ways: P1-domain in first and BP7-domain in first. For the spontaneous insertion case, BEAM molecules were initially placed near the expanded gap, both parallel to the stack edge and/or situated above the top-most sheet. Simulations were then conducted to test if those BEAM molecules could spontaneously insert into the gap. In each scenario, six BEAM molecules were placed in the periodic simulation cell in different arrangements, along with the graphite stack (in the expanded gap configuration) and liquid water. The peptide positions were initially frozen to ensure the ingress of water molecules into the expanded gap, prior to running production simulations in which the peptides were free to move. Ten independent simulations were run for 150 ns for each such arrangement.

As was previously reported for the parent P1 peptide, all spontaneous insertion tests ended with the expanded gap remaining in place at the end of simulations, in which at least two BEAM molecules were found to remain inserted into the gap. Next, based on the simulations from the second case, the spontaneous insertion mechanism for the BEAM was found to be reminiscent of the P1-based mechanism, namely via a sideswiping movement (Figure B2.2a), indicating the capability of the BEAM to find the solvent-accessible surface of the graphene sheet and bind onto it by moving into the gap. In addition, during the insertion progress of the biomolecules, the detached graphene sheet was observed to have a greater mobility of rotation and/or large tilting angle caused by the local assembling of BEAMs within the gap, whereas the top sheet in BEAM-free tests lacked such flexibility, which may also contribute to the exfoliation progress under sonication.

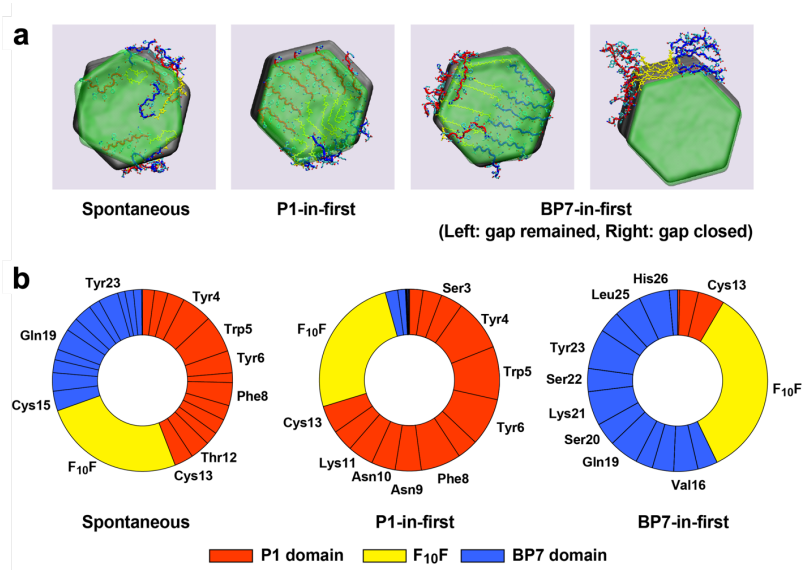

Fig. B2.2. a)Exfoliation initial stages: expanded gap stability and BEAM insertion. Snapshots of the results of BEAM spontaneous insertion and pre-insertion tests for different scenarios having the P1 domain in the gap first, pre-insertion test having the BP7 domain in the gap first, and one instance of the BP7 domain in the gap first for which the gap closed. The top-most sheet is rendered in transparent green, the P1 peptide backbones are shown in red, BP7 peptide backbones are blue and the $F_{10}F$ chains are in yellow. Water is not shown for clarity. b). Decomposition analysis of BEAM atoms located within the expanded gap region.

For the pre-insertion runs, in most instances the expanded gap remained open. For the P1-in-first or BP7-in-first cases, the majority of the pre-inserted peptide domain remained within the gap, together with nearly all of $F_{10}F$ and part of the other peptide domain

adsorbed into the gap as well (Figure B2.2b). The packing of BEAMs within the gap showed some evidence of partial ordering for the pre-insertion cases. However, the spontaneous insertion tests resulted in a quite diverse arrangement of those conformations within the gap. Further analysis of which parts of the BEAM remained inside the gap using the last frame of the spontaneous insertion test trajectories for each production run revealed that a greater number of P1 domain atoms were found in the gap compared with the BP7 domain, consistent with the slightly higher binding affinity for P1 on graphene over BP7. Together with the 60% success rate of pre-insertion tests performed with BP7 domains placed in the gap first, this indicates that the BP7 domain was certainly able to be inserted into the gap as long as this included the presence of the exfoliant domain (P1) or linker ($F_{10}F$). More specifically, residues including the YWY motif and the phenylalanine residue in the P1 domain, and the tyrosine residues in the BP7 domain, clearly acted as the main binder of the BEAM as well as the $F_{10}F$ hydrocarbon spacer. All of these results suggested that the BEAM is able to exfoliate the graphite under sonication conditions, similar to the behavior of P1 or $P1CF_{10}$ in experiment.

With the computational analysis indicating that the BEAM can support graphene exfoliation, its use in liquid phase graphene exfoliation was analyzed experimentally. Previous binding studies confirmed that the BEAM can bind the graphene surface with a ΔG value of -35.3 ± 1.9 kJ/mol. For graphene exfoliation, 1 mg of the BEAM was dissolved in 10 mL of water to which 50 mg of bulk graphite was added. This mixture was then subjected to probe ultra-sonication for 1 h. After sonication, the sample was centrifuged to separate bulk graphite where the supernatant containing the exfoliated graphene sheets was collected for further characterization.

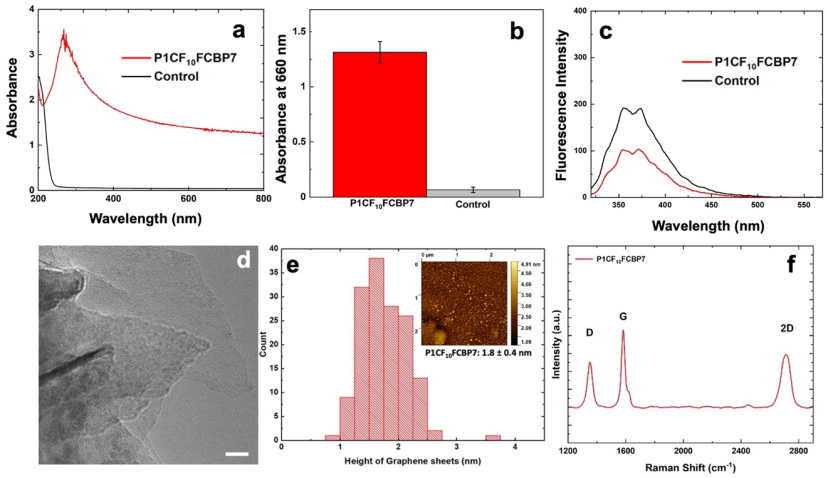

Fig. B2.3. Characterization analysis of the exfoliated sheets using the BEAM molecule. a) Absorbance measured at 660 nm of the exfoliated graphene samples. b) UV-vis spectra of the exfoliated graphene samples. c) Fluorescence intensity of the BEAM molecule and exfoliated graphene sample. d) TEM image of BEAM-exfoliated graphene sheets, scale bar represents 20 nm. e) AFM image of BEAM-exfoliated graphene sheets with the height distribution. f) Characterization of graphene sheets using Raman spectroscopy.

UV-vis spectroscopy was initially used to quantify the degree of exfoliation achieved as shown in Figure B2.3a and b. From the supernatant of the exfoliated sample, a dark solution was achieved, which demonstrated substantial scattering in the sample (Figure B2.3a), consistent with significant exfoliation. When the same sonication procedure was performed in the absence of the BEAM, a clear and colorless solution was achieved, which demonstrated negligible absorbance. To further compare the samples, the degree of scattering at 660 nm was compared (Figure B2.3b), giving rise to a value of 1.31 ± 0.098 and 0.065 ± 0.024 cm^{-1} for the reactions with and without the BEAM present, respectively, confirming significant graphene exfoliation using the biomolecules.

In addition to UV-vis analysis, fluorescence spectroscopy of the sample before and after exfoliation was studied (Figure B2.3c). The BEAM is generally fluorescent with an emission at 378 nm due to the aromatic residues within the peptides. As the BEAM is bound to the surface of graphene, quenching of the fluorescence intensity was observed, consistent with previous studies. This suggests that the BEAM molecules are adsorbed to the graphene surface to maintain material colloidal stability.

Imaging of the exfoliated graphene sheets was achieved using both transmission electron microscopy (TEM) and atomic force microscopy (AFM). Figure B2.3d shows a TEM image of a single graphene sheet exfoliated using the BEAMs. Significantly large samples were obtained with lateral dimensions of greater than 100 nm. AFM analysis was also conducted to complement TEM imaging to measure and assess the thickness of the graphene sheets. Figure B2.3e shows the AFM image of the graphene sample exfoliated by the BEAM and the statistical analysis of the height profiles. The average height of the BEAM-exfoliated material was 1.8 ± 0.4 nm, which is similar to the thickness of the samples exfoliated with the parent P1 peptide previously.

In addition, Raman spectroscopy analysis was conducted to provide insights into the defect density. This was done by depositing the exfoliated graphene sheets onto a gold-coated glass slide and exciting at 514.5 nm. Figure B2.3f displays a Raman spectrum averaged by collecting spectra from at least six spots from the BEAM-exfoliated graphene sheets. Three peaks can be observed in the spectrum at 1350, 1585, and 2720 cm^{-1}, corresponding to the D, G and 2D peaks, respectively. The G peak represents in-plane stretching vibrations involving the sp^2 hybridized carbon atoms. The D peak corresponds to lattice defects and the 2D peak is the overtone of the D peak resulting from two phonon vibrations within the lattice. The intensity and shape of the 2D peak is known to correlate to the number of graphene layers. While we do not observe a single sharp high intensity 2D peak corresponding to monolayer graphene, the lineshape and intensity of the 2D peak in Figure B2.3f suggests the presence of few layers of graphene. To determine the quality of the graphene sheets, the (integrated) intensity ratio between the D peak and the G peak (I_D/I_G) can be used. The ratio calculated for the graphene sheets exfoliated by BEAM is 0.57 ± 0.12 which is higher than the ratio previously measured for P1 ~0.4, suggesting more defects on the surface.

The post-sonication stability of the exfoliated graphene is achieved via BEAM adsorption onto the nanosheets; this sterically prevents recombination of the materials to regenerate the bulk system. To explore this effect, the free energy profile of the reunification of two BEAM-decorated graphene sheets in liquid water was examined computationally. The two sheets were arranged in a face-to-face configuration. These simulations were conducted to mimic post-sonication events at 300 K, using the umbrella sampling MD simulation method. Following a procedure similar to that previously published to investigate the free energy profile for the face-to-face approach of two P1-decorated sheets, extensive tests were first conducted to determine an appropriate level of loading (*i.e.*, how many BEAM molecules could be loaded onto the ~7.5 nm diameter graphene sheet). The BEAM-loading test simulations determined a maximum stable loading of 12 BEAMs distributed over both sides (six per side) of the graphene sheet, resulting in a *pseudo*-film thickness of ~1.5 nm. The two BEAM-decorated sheet complexes were then arranged face-to-face and separated vertically with the closest distance between two complexes being ~2.5 nm (between a BEAM atom on sheet one/BEAM atom on sheet two) while the initial centre-to-centre distance between the two graphene sheets was ~5.5 nm (Figure B2.4a).

The potential of mean force (PMF) profile for the decorated-sheet reunification is shown in Figure B2.4b with representative snapshots of the system at different values of the reaction coordinate (RC, the vertical center-to-center distance between the two graphene sheets). Similar to what was previously reported for the PMF profile of two P1-decorated graphene sheets, two apparent regimes were present: the low-repulsion region and the high-repulsion region with the transition point for a value of the RC of ~2.5 nm. The free energy penalty for the two complexes to approach each other at a distance greater than 2.5 nm inter-sheet separation was minimal. However, an abrupt onset indicating a repulsion effect was observed when the two complexes approached more closely than this, which was attributed to the close contact between the BEAM molecules absorbed on the opposing graphene surfaces. This made the reunification of the two graphene sheets extremely unlikely. Between the RC values of 2.5 to 1.0 nm, no entire BEAM chain was observed to be squeezed out the inter-sheet gap, whereas parts of the BEAMs were forced from the gap with different expulsion rates as indicated in Figure B2.4c. Compared with the P1 domain, the BP7 domains were more readily expelled from the gap with a higher expulsion rate, as indicated by the number of atoms belonging to the BP7 domains decreasing more rapidly. The $F_{10}F$ domain had the slowest expulsion rate, indicating its strong binding affinity. Water molecules were always observed to be found in the gap, even at the very close inter-sheet separations with higher repulsion. However, the total number of water molecules also decreased as the inter-sheet gap decreased; therefore, one source of the high-repulsion regime could be attributed to effective dehydration in the gap leaving only a highly-dehydrated BEAM layer in the center. As such, similar to its parent P1 peptide, the BEAM molecule exhibited similar behavior in the post-sonication scenario in that the BEAM-decorated graphene sheets were able to inhibit reunification in the aqueous environment to maintain the long-lived dispersions of exfoliated graphene sheets.

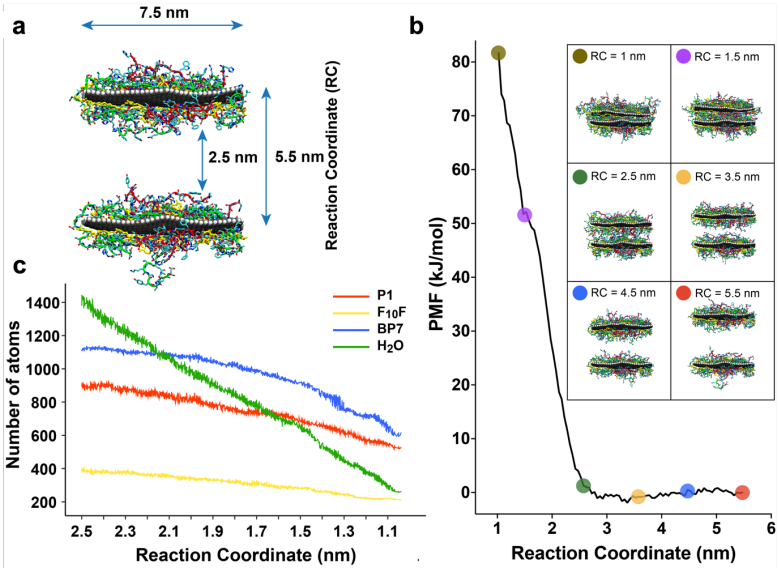

Fig. B2.4. Sheet reunification study using umbrella sampling simulations. a) Set-up of the sheet reunification umbrella sampling simulations shown in side view; the two BEAM-decorated sheets with one placed above the other with an initial inter-sheet separation of 5.5 nm. P1 peptide backbones are shown in red, $F_{10}F$ group in yellow, and BP7 backbones in blue. Water is omitted for clarity. b) Potential of mean force profile for two BEAM-decorated graphene sheets approaching each other face-to-face in water. The reaction coordinate is defined as the vertical sheet-to-sheet separation. Colored circles indicate snapshots (shown as insets) at different inter-sheet separations. c) The evolution of number of atoms within the gap between the two graphene sheets as a function of reaction coordinate from 2.5 nm to 1.0 nm.

In summary, this work has demonstrated that the newly proposed hybrid molecule, BEAM, was able to bind the solvent-exposed graphene surface in a similar manner to the P1 peptide or the fatty acid conjugated molecule $P1CF_{10}$ to both enable the exfoliation of the graphene sheets under sonication conditions and stabilize the resultant colloidal suspension of the graphene sheets in water. This suggests that incorporation of additional functionality (*e.g.*, the BP7 peptide) into the biomolecular construct does not interfere with

graphene exfoliation. The results further suggest a stronger interaction between the P1 domain of the BEAM with the graphene surface, as anticipated from the original target affinity of the peptide. This indicates that the BP7 domain may remain available for *h*-BN binding for eventual heterostructure formation. Significant more experimental analysis is required to achieve and confirm such capabilities.

B3. Variation of BEAM Sequence and Effects on Binding and Exfoliation.

While the synthesis of the BEAM bifunctional, P1CF$_{10}$FCBP7, was discussed above, a facile synthetic approach to fabricate the variants, BP7CF$_{10}$FCP1, P1CF$_{10}$FCP1, and BP7CF$_{10}$FCBP7, was developed. The synthesis started by fabricating the modified fatty acid spacer, F$_{10}$F, which was done by replacing both terminal chlorides in sebacoyl chloride with maleimide groups. Once the fatty acid spacer was synthesized, each peptide was coupled sequentially by adding one at a time. The peptides containing a cysteine on the C-terminus, P1C and BP7C, were first coupled to one of the maleimide groups. After the first coupling step, the second peptide, either CP1 or CBP7 was added to the bioconjugate to produce the final product. The obtained product after each coupling step was purified by reverse phase HPLC and confirmed by MALDI-TOF mass spectroscopy.

Binding analysis of the BEAM variants, BP7CF$_{10}$FCP1, P1CF$_{10}$FCP1, and BP7CF$_{10}$FCBP7, onto graphene were studied using QCM. This technique has been widely used in previous studies to observe and quantity the binding affinity of peptides onto a target surface (*e.g.*, AuBP1 peptide onto Au). The Au sensors were coated with a single layer of graphene using previous methods. The frequency change was observed as aqueous solutions of the bifunctionals ranging in concentration (7.5-17.5 µg/mL) were flowed over the QCM sensor surface. Due to the Sauerbrey relation, the change of frequency is directly related to the change of mass. This suggests that the bifunctional molecules are adsorbed to graphene when there is an increase of change of frequency. Figure B3.1a shows the inverted change of frequency measurement as BP7CF$_{10}$FCP1 was flowed over the graphene surface. The frequency change was then fit using the Langmuir isotherm yielding k_{obs} values. These values are then plotted as a function of concentration with a line of best fit, as shown in Figure B3.1b. For this, the rate of adsorption (k_a) and rate of desorption (k_d) can be extracted from the slope and y-intercept, respectively. The equilibrium constant (K_{eq}) can be obtained from k_a/k_d, which is then used for the calculation of the free energy of binding (ΔG) for the graphene surface.

The binding affinity values for the BEAM bifunctionals, P1CF$_{10}$FCBP7, BP7CF$_{10}$FCP1, P1CF$_{10}$FCP1, and BP7CF$_{10}$FCBP7 obtained from QCM measurements are listed in Table B3.1. The QCM analysis and measurements of the original BEAM molecule, P1CF$_{10}$FCBP7, was previously reported and found to be -35.3 ± 1.9 kJ/mol. When the placement of the peptides was reversed to obtain the BP7CF$_{10}$FCP1 bifunctional the binding energy changed to -31.9 ± 1.8 kJ/mol. Additionally, when the bifunctional only comprised of the P1 peptide, P1CF$_{10}$FCP1, the ΔG value was calculated to be -36.9 ± 3.0 kJ/mol. This was notably higher when the bifunctional only contained the BP7 peptide on each side, BP7CF$_{10}$FCBP7, where the ΔG value was -31.3 ± 1.3

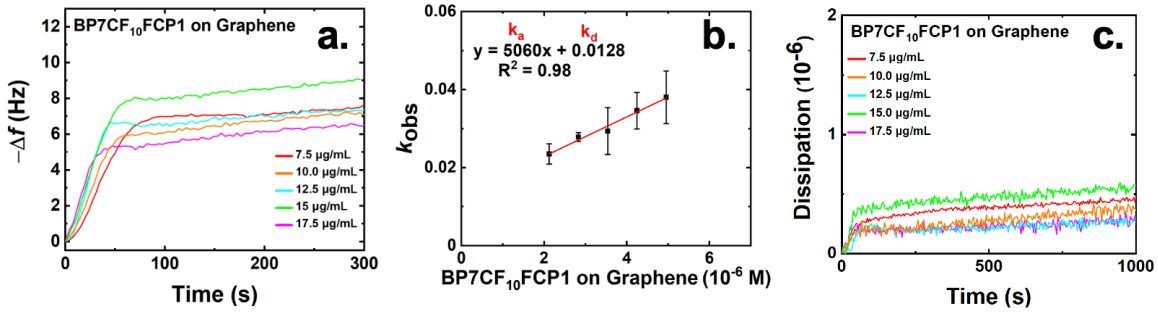

Fig. B3.1. QCM analysis of BP7CF$_{10}$FCP1 on graphene. (a) frequency change during binding over time for a range of concentrations. (b) plot of the k_{obs} obtained as a function of concentration. (c) Dissipation energy generated over time for various concentrations.

kJ/mol. Interestingly, the binding energies calculated for the bifunctionals with the BP7 peptide attached on the N-terminus suggest a diminished affinity for graphene. However, it could also be assumed that the binding affinity towards graphene increased when the P1 peptide was attached on the N-terminus of the bifunctional. These results indicate that these bifunctionals have the ability to bind to the graphene and the ordering of the peptides does have an effect on the binding affinity.

Table B3.1. Free energy of binding (ΔG) and maximum dissipation energy for each bifunctional during adsorption to graphene.

Bifunctional	*ΔG (kJ/mol)*	Maximum Dissipation Energy (u)
$P1CF_{10}FCBP7$	-35.3 ± 1.9	0.72
$BP7CF_{10}FCP1$	-31.9 ± 1.8	0.86
$P1CF_{10}FCP1$	-36.9 ± 3.0	4.87
$BP7CF_{10}FCBP7$	-31.3 ± 1.3	0.65

Additionally, QCM analysis can also provide the dissipation energy of the bio-overlayer formed on the graphene surface during adsorption. An increase of dissipation energy during binding suggests an increase in the viscoelastic behavior on the surface. Figure B3.1c shows the dissipation energy over time as the $BP7CF_{10}FCP1$ bifunctional adsorbs to the graphene surface. This increase was seen for all bifunctional variants indicating a more viscoelastic overlayer. The maximum dissipation energy measured for each of the bifunctional variants is listed in Table B3.1 with $P1CF_{10}FCP1$ exhibiting the greatest viscoelasticity with a value of 4.87. Previous QCM binding studies of BP7 and P1 on graphene showed that the dissipation energy was negligible, indicating a rigid monolayer was formed during adsorbing. Interestingly, the same negligible dissipation energy was observed when P1 was modified with fatty acids with carbon chain lengths from 6-10 on either the C- or N-terminus. However, when the 12-carbon fatty acid was added to P1, an increase of dissipation energy was measured. Similarly, recent studies showed that the addition of the same carbon fatty acids ranging from 6-12 carbon chain lengths onto BP7 created a more viscoelastic overlayer during adsorption to *h*-BN. The size of the biomolecules when the fatty acid is incorporated can have an impact on the dissipation energy, which can also be seen for the bifunctional variants since the size is nearly doubled with the attachment of a second peptide.

To complement the QCM binding analysis, AFM was also employed to image the bio-overlayer formed with the bifunctionals on the graphene surface. The graphene surface used for AFM was highly oriented pyrolytic graphite (HOPG). HOPG is a common graphene interface used in previous AFM studies of binding of peptides onto graphene. Prior to imaging, aqueous solutions of the bifunctional molecules were drop-casted on the cleaved HOPG surface and left to adsorb for 15 mins. After the surface was rinsed and dried, it was imaged in tapping mode. The AFM image of the bio-overlayer formed with $BP7CF_{10}FCP1$ on the HOPG is shown in Figure B3.2a. When examining the zoomed in area of the surface in Figure B3.2b, the peptides seemed to

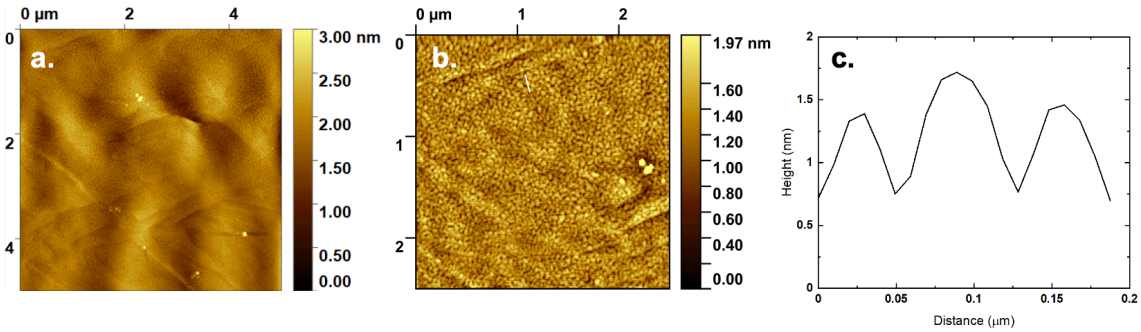

Fig. B3.2. AFM analysis of $BP7CF_{10}FCP1$ bifunctional overlayer on HOPG. (a) large area scan, while (b) is a zoomed-in image of the surface. (c) height profile obtained for the area indicated in the middle image.

aggregate and form a dense network that had a height of ~0.8 nm. Areas of uncoated regions were observed which enabled the measurement of the height of the peptide overlayer, shown in Figure B3.2c.

The same high coverage and morphology was consistent for the other two variants, P1CF$_{10}$FCP1 and BP7CF$_{10}$FCBP7, but with larger overlayer heights of ~1.3 nm and ~2.1 nm, respectively. Conversely, the previously reported AFM images of the original BEAM molecule, P1CF$_{10}$FCBP7 on HOPG showed a higher level of coverage comprised of few pores of uncoated peptide regions that were small in size. The height of the peptide overlayer was higher than the variants, ~3.5 nm. Variations in the morphology of the peptide overlayer on HOPG could be a direct result of the order of the peptides which can affect the peptide aggregations formed.

The QCM and AFM studies provided clear evidence that the BEAM molecule and variants have the ability to recognize and bind to the graphene surface. Further studies can be made to observe whether the bifunctionals can drive exfoliation of graphene and stabilize the sheets in solution. For this, a solution comprised of 1 mg of bifunctional molecule and 50 mg of graphite in 10 mL of water was subjected to tip-type probe ultra-sonication. Sonication was employed with a 0.25 in titanium tip for 1 h at a pulse rate of 3s/3s at 100% amplitude. After sonication, the sample was subjected to centrifugation in which the supernatant containing the exfoliated graphene sheets was collected to separate the unexfoliated bulk graphite. The supernatant was then fully characterized (Table B3.2).

Table B3.2. Characterization analysis of the exfoliation sheets using the various bifunctionals.

Bifunctional	*A/l m^{-1}*	*Size (nm)*	*Zeta (mV)*	Height (nm)	*D/G*
P1CF$_{10}$FCBP7	131.3 ± 9.8	135.1 ± 4.5	-39.0 ± 1.3	1.8 ± 0.4	0.57 ± 0.12
BP7CF$_{10}$FCP1	150.3 ± 8.0	137.4 ± 3.1	-40.5 ± 1.5	1.4 ± 0.4	0.47 ± 0.07
P1CF$_{10}$FCP1	147.4 ± 6.7	136.4 ± 2.4	-39.4 ±. 3.2	1.7 ± 0.6	0.44 ± 0.05
BP7CF$_{10}$FCBP7	107.3 ± 24.1	123.8 ± 2.5	-44.6 ± 1.2	2.0 ± 0.6	

The collected supernatants containing exfoliated graphene sheets were analyzed via UV-vis spectroscopy to determine the degree of exfoliation. An increase in absorbance was observed when incorporating the bifunctionals into the sonication process indicating successful graphene exfoliation. When the same sonication procedure with similar conditions was performed in the absence of the bifunctionals, a low absorbance was measured corelating to no graphene exfoliation observed. When comparing the degree of exfoliation by the amount of absorbance measured at 660 nm (Figure B3.3a and b) the bifunctionals, P1CF$_{10}$FCBP7, BP7CF$_{10}$FCP1, and P1CF$_{10}$FCP1 showed identical degrees of exfoliation. However, the bifunctional, BP7CF$_{10}$FCBP7, showed the lowest scattering of 107.3 ± 24.1 m^{-1}, indicating a lower degree of exfoliation. This might be

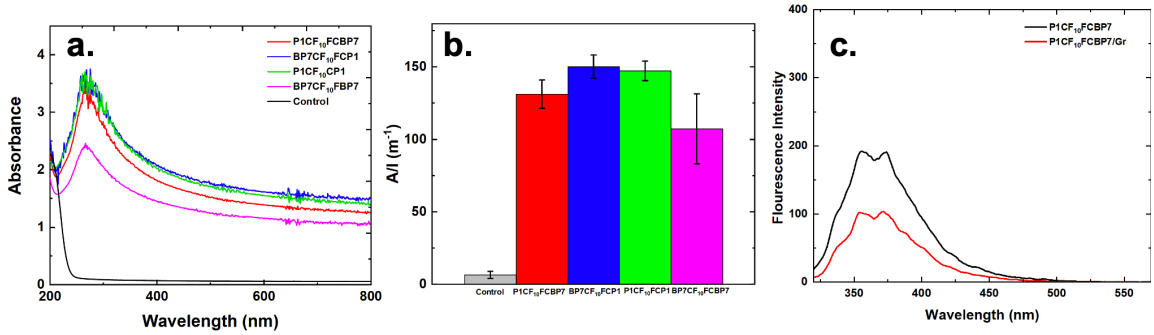

Fig. B3.3. Analysis of the exfoliated graphene sheets. Part (a) presents the UV-vis spectra of the exfoliated graphene samples, while part (b) compares of the absorbance intensity at 660 nm. The fluorescence intensity of P1CF$_{10}$FCBP7 alone and P1CF$_{10}$FCBP7-exfoliated graphene sheets is shown in part (c).

explained by the lower binding affinity BP7 has towards the graphene surface compared to P1. Regardless, all for the bifunctionals demonstrated the ability to produce exfoliated graphene sheets during sonication.

Furthermore, DLS analysis was employed indicating similar sizes of the graphene sheets obtained with no significant change between the bifunctionals. The size obtained from using all the bifunctionals fell in a range of 120-140 nm. The average size of the sheets resulting from the exfoliation driven by the BP7CF$_{10}$FCBP7 bifunctional was measured to be 123.8 ± 2.5 nm which was lower than the other bifunctionals that had an average size measured between 135.1-137.4 nm. Further characterization via fluorescence spectroscopy (Figure B3.3c) showed the fluorescence intensity of the P1CF$_{10}$FCBP7 bifunctional alone in solution and the graphene sheets exfoliated with the biomolecules. The bifunctional molecules typically fluorescence with an emission at 378 nm due to the aromatic residues within the peptides. As the bifunctional is bound to the surface of graphene, a quenching of the fluorescence intensity was observed, consistent with the peptides remaining adsorbed to the graphene surface, thus stabilizing the sheets in solution.

Imaging of the exfoliated graphene sheets via TEM was employed. Figure B3.4a shows a TEM image of a single graphene sheet exfoliated with P1CF$_{10}$FCBP7 bifunctional with lateral dimensions > 100 nm. Furthermore, AFM analysis was conducted to complement TEM imaging by measuring the thickness of the graphene sheets. Figure B3.4b shows the AFM image of the graphene sheets exfoliated by P1CF$_{10}$FCBP7 while Figure B3.4c displays the statistical analysis of the height profiles. The average height of the graphene sheets for the P1CF$_{10}$FCBP7 system was calculated to be 1.8 ± 0.4 nm. The average heights of the graphene sheets obtained for the variants, BP7CF$_{10}$FCP1, P1CF$_{10}$FCP1, and BP7CF$_{10}$FCBP7 can be found in Table 2 and were measured to be 1.4 ± 0.4, 1.7 ± 0.6 and 2.0 ± 0.6 nm, respectively. The averages for all bifunctionals indicate that the thickness of the sheets was similar with a majority <2.5 nm in thickness. Additionally, these measurements confirms that the bifunctionals were successful in exfoliating graphite to single or few layered graphene sheets.

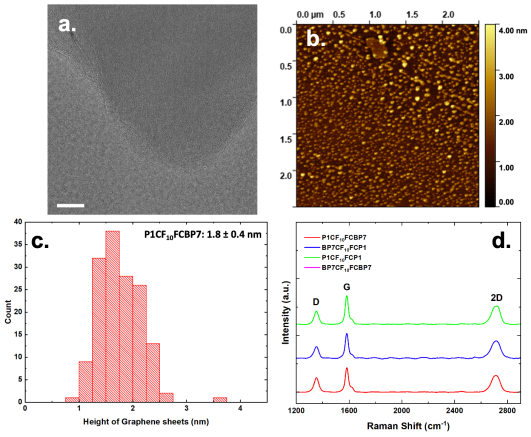

Fig. B3.4. (a) TEM image of P1CF$_{10}$FCBP7-exfoliated graphene sheets (scale bar = 20 nm). (b) AFM image of P1CF$_{10}$FCBP7-exfoliated graphene sheets. (c) Height distribution of P1CF$_{10}$FCBP7-exfoliated graphene sheets. (d) Characterization of graphene sheets using Raman spectroscopy.

In addition, Raman analysis was conducted to further characterize the graphene sheets providing insight to the defect density. This was done by depositing the exfoliated materials onto a gold-coated glass slide and exciting at 514.5 nm. Figure B3.4d displays the Raman spectra of the graphene sheets obtained with each bifunctionals, P1CF$_{10}$FCBP7, BP7CF$_{10}$FCP1, and P1CF$_{10}$FCP1. From the Raman spectra, three peaks were present, the D, G, and 2D at 1350, 1585, and 2720 cm^{-1}, respectively. The G peak represents the stretching vibration occurring in-plane involving the sp^2 hybridized carbon atoms. Additionally, the D peak corresponds to the defect band or disorder band since the intensity of the band is directly proportional to the levels of defects. The third band, the 2D peak, is an overtone of the D peak resulting from two phonon vibration within the lattice. While the 2D band does not provide information about the defects, it does correlate to the number of graphene layers. The line width of the 2D peak observed for each graphene

exfoliation sample suggests materials of a few layers of graphene were produced. To determine the quality of the graphene sheets, the intensity ratio between the D peak and the G peak (I_D/I_G) can be used (Table B3.2). The ratios observed for the samples fell within a range of (0.44-0.57) which is higher than the ratio measure for P1 of ~0.4. The highest ratio observed was for the original BEAM, P1CF$_{10}$FCBP7, measured at 0.57, suggesting that there are more defects within this sample.

Molecular dynamics (MD) simulations were used to explore the exfoliation mechanisms and capabilities of the BEAM variant molecules. Similar to the approach described in Section B2, MD simulations were used to examine the possibility and mechanisms of dynamic insertion of the BEAM molecules into the expanded gap region between two graphene sheets, and the ability of the BEAMs to maintain this gap beyond the timescale it takes for the gap to close in their absence (~ 90 ns), all done in the medium of liquid water. This process is representative of the first stage of graphene exfoliation from bulk graphite in aqueous media and is a necessary, but not sufficient, test to explore exfoliation capability. As in Section B2, a model of a nine-layer graphite stack (sheet diameter ~ 7.5 nm) was prepared and the gap between the top two graphene sheets in the stack was expanded to 10 Å to mimic the expanded gap under sonication conditions, in the presence of the BEAM variant molecules in the NVT ensemble. Only the very bottom graphene sheet was frozen in space and the rest of the sheets in the stack, including the top-most partially detached sheet, were completely free to move. Simulation details were the same as described in Section B.3. As overviewed in Section B2, two different types of simulations were performed: "pre-insertion" simulations where six chains of the BEAM are initially placed inside the expanded gap (testing to see if the BEAMs can remain with the gap over a 100 ns timescale), and "spontaneous insertion" simulations, where the six BEAMs are placed nearby to the graphite stack to test if the BEAMs can spontaneously intercalate into the expanded gap. In each scenario, six BEAM molecules were placed in the periodic simulation cell in different arrangements, along with the graphite stack (in the expanded gap configuration) and liquid water. In the initial setup for the "pre-insertion" simulations, the BEAM molecule is slightly longer than the diameter of the graphene sheets in the stack, such that when the BEAMs are inserted into the gap, some part of the molecule must protrude outside of the graphite stack. In this case, for the BP7CF$_{10}$FCP1 BEAM, the molecule was inserted either with P1-domain in first or BP7-domain in first, to explore all possibilities. The BEAM atomic positions were initially frozen to ensure the ingress of water molecules into the expanded gap, prior to running production simulations in which the peptides were free to move.

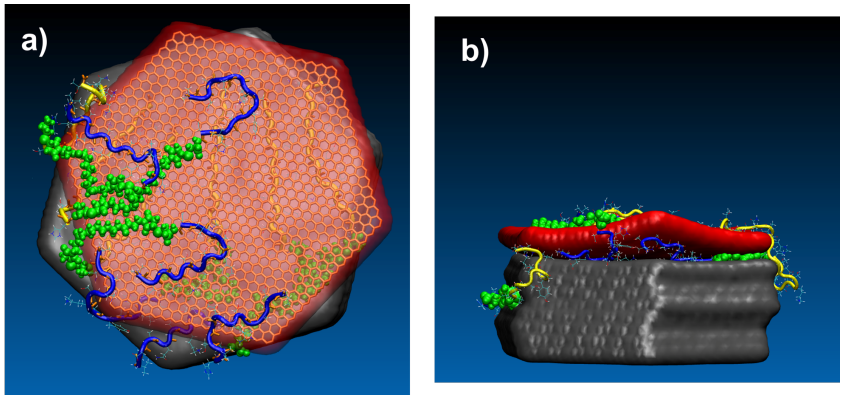

Fig. B3.5. Example outcomes of MD simulations of the initial stages of graphene exfoliation with BEAM variants. Top graphene layer in stack shown in red, remaining graphite stack shown in grey. Example BEAM shown is BP7CF$_{10}$FCP1, with BP7, F$_{10}$F and P1 domains shown in blue, green, and yellow respectively. Water not shown for clarify. (a) Top view of graphite stack indicating retention of "pre-inserted" BEAM molecules which enable the expanded gap to remain open. The top graphene layer is rendered translucent to enable visualization of the intercalated chains. (b) Side view of the graphite stack following a "spontaneous insertion" simulation, highlighting how the BEAM chains have entered into and remained inside the expanded gap.

Three independent simulations were run for 100 ns for each such arrangement.

As was reported for the original BEAM in Section B2, all pre-insertion and spontaneous insertion MD simulations resulted in the retention of the expanded gap in the graphite stack, with at least one BEAM molecule being involved in bracing this gap open over the 100 ns timescale. Example snapshots of the initial and final configurations of the pre-insertion and spontaneous insertion runs are shown in Figure B3.5. These simulation data are consistent with the experimental findings that all BEAM variants are able to support graphene exfoliation to approximately a very similar degree.

In conclusion, this study shows the effects of the order of the peptide within the bifunctionals on the binding affinity to the graphene surface and the exfoliation of graphene nanosheets from bulk graphite. The order of the peptides had a slight impact on the binding affinity, showing a diminished affinity for graphene when the BP7 is attached on the N-terminus while the affinity increased when the P1 peptide was attached to the N-terminus. Additionally, each bifunctional was shown to have the ability to exfoliate graphene regardless of the peptide order, as supported by evidence from molecular dynamics simulations. The size and height of the sheets were not affected and all bifunctionals appeared to produce identical quantity of graphene sheets with similar quality. These findings provide insight into the exfoliation of nanomaterials and demonstrate the possibility to use these bifunctional molecules to recognize and assembly heterostructures comprised of other nanosheet structures.

B4. Sustainable, Aqueous Exfoliation of MoS_2 via Bio-inspired Avenues.

To fully explore the potentially transformative application of transition metal dichalcogenides (TMDs), the ability to sustainably access these two dimensional (2D) materials must be identified that allows for the acquisition of high quality structures with minimal defects. One TMD that has been extensively studied for its electronic properties is MoS_2. To produce MoS_2 nanosheets, exfoliation of the bulk stacked structure has been used. During exfoliation, defects such as sulfur vacancies, may occur, which can be used to covalently functionalize the surface. Unfortunately, such defects and functionalization can lead to diminished electronic properties. An ideal approach to overcome the negative effects of covalent ligand attachment is through the use of surface passivants that non-covalently adsorb onto the MoS_2 surface. Recently, Chen and co-workers have identified a peptide that non-covalently binds to MoS_2, which was termed MoSBP1 (YSATFTY). Examination of both the native peptide and the end-capped version (acylated N-terminus and amidated C-terminus) demonstrated MoS_2 surface binding through atomic force microscopy (AFM) and molecular dynamics (MD) simulation. From the AFM images, the MoSBP1 peptide appeared to form an elongated linear structure on HOPG, a graphene surrogate, and MoS_2, showing preferred growth along the (100) facet of MoS_2. Although such results demonstrate that the MoSBP1 peptide binds the MoS_2 surface, its use to generate high quality individual sheets was not assessed.

TMDs such as MoS_2 have been exfoliated through sonication in water or organic solvents. Typically, the exfoliation process requires the presence of ligands to stabilize and prevent the reassociation of individual exfoliated sheets back into their bulk stacked arrangement. Peptides are viable bio-based ligand candidates that can be used in aqueous media. Additionally, peptide assisted sonication is a low cost exfoliation method that produces little to no chemical waste, allowing for potentially sustainable routes to generate TMD nanosheets. In this regard, peptides have been previously explored for aqueous sonication-based exfoliation of 2D materials such as graphene, in which the aromatic rings in the peptide residues can support for $\pi-\pi$ interactions with the surface. Such non-covalent interactions can preserve the chemical and physical integrity of the 2D nanosheets and the electronic character of the surface.

While notable work has been done on peptide-based graphene exfoliation, only very limited studies have examined peptide-driven exfoliation of MoS_2 in aqueous media. To this end, the exfoliation of MoS_2 using was reported using cross-β-amyloid nanotubes that produced high quality 2-to-4 layered sheets. While MoS_2 nanosheets were achieved, large, peptide-based structures were exploited for the exfoliation process. Further investigation of the effects of short, individual peptides for exfoliation suggest that peptide-driven exfoliation approaches are promising and may lead to a new and innovative top-down approaches to generating MoS_2 sheets.

Here, the exfoliation of individual sheets of MoS_2 from bulk systems in aqueous solution is demonstrated using the MoSBP1 peptide where the effect of end capping is explored. The exfoliation process was studied both experimentally and via computational simulations to provide atomically-resolved understanding of the interactions between the biomolecules and TMD surface that drive the process. For exfoliation, the peptides and bulk MoS_2 were commixed in water and bath sonicated. The quality and quantity of MoS_2 nanosheets produced were compared between the parent MoSBP1 peptide and the capped variant (termed CMoSBP1). Once exfoliated, the isolated nanosheets were fully characterized via UV-vis, FT-IR, and Raman spectroscopies, AFM, Zeta Potential analysis, and high-resolution transmission electron microscopy. To complement the experimental observations, MD simulations were conducted to give more details at the atomic levels to the mechanisms of exfoliation processes and stability of exfoliated MoS_2 nanosheets. The

simulation data were also employed to shed light on nanostructures of MoS_2 sheets experimental observed.

To drive peptide-assisted MoS_2 exfoliation, a low-energy bath sonication approach was adapted from prior studies employed for graphene exfoliation. Briefly, an aqueous solution of the peptide (5 mL at 0.1 mg/mL) was prepared where the solution was sonicated for 2 min to facilitate peptide dissolution. This step was important due to the known limited solubility of the capped CMoSBP1 biomolecule. Once dissolved, 50 mg of the bulk MoS_2 powder was added to the mixture, which was sonicated in a bath sonicator for 6 h. It is important to note that the exfoliation efficiency was highly sensitive to the position of the vial in the bath sonicator; the reaction must be positioned at the point of maximum sonication in the system, as previously demonstrated. Once the exfoliation process was complete, the system was centrifuged to remove any remaining bulk MoS_2 powder where the exfoliated samples remain suspended in the supernatant. These materials were subsequently characterized.

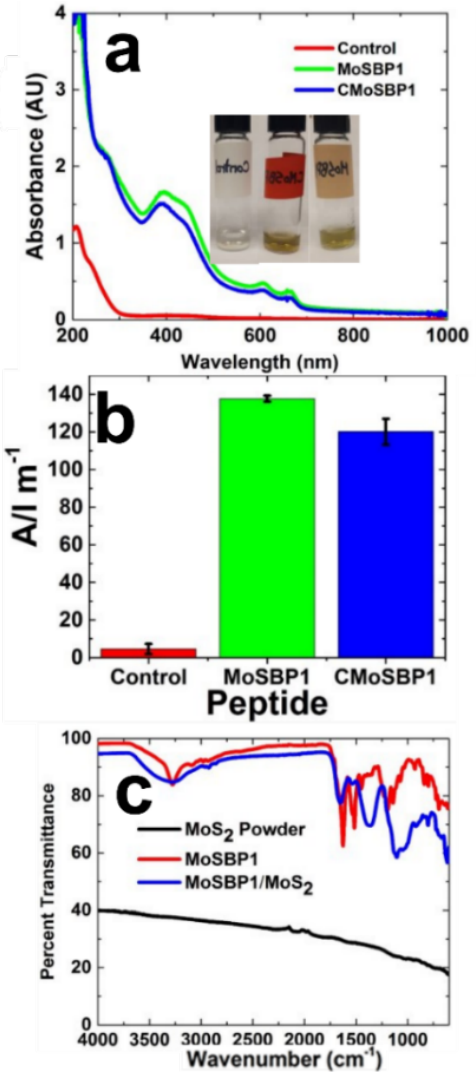

Fig. B4.1. Spectroscopic analysis of peptide-driven MoS_2 exfoliation. (a) UV-vis spectra of the exfoliated materials where the insert displays images of the reaction system. (b) Comparison of absorbance values at 348 nm for the reactions in panel (a). (c) FT-IR analysis of the exfoliated materials achieved using the indicated peptide.

UV-vis analysis enabled the comparison of MoS_2 exfoliation efficiency conferred by the MoSBP1 and CMoSBP1 peptides (Figure B4.1a). For comparison, images of the exfoliation supernatant are presented in the inset of Figure B4.1a, demonstrating a yellow solution for the reactions where peptides were present. This color, which was different than for the bulk powder that was gray, was consistent with prior MoS_2 exfoliation systems. A separate control exfoliation, in which bulk powder was sonicated in water in the absence of any biomolecule, was performed under the same sonication conditions. For the peptide-driven reactions, nearly identical UV-vis spectra were observed with four distinct peaks at ~390, ~450, ~610, and ~660 nm. The two peaks at < 500 nm correlated to the direct transition from deep within the valance band to the conductive band at the *M* point in the Brillouin zone. The two smaller peaks located at >500 nm are consistent with the excitation transition of the *K* point. The presence of these peaks indicated successful peptide-assisted exfoliation of 2H MoS_2 sheets with both CMoSBP1 and MoSBP1. This is significant because previously reported biomolecule-based aqueous exfoliation of MoS_2 required the formation of peptide nanotubes to produce the MoS_2 nanosheets, whereas this was successfully accomplished here using a seven residue peptide.

In the absence of peptide, this system did not exhibit any significant absorbances at

wavelengths > 300 nm; however, there were minor, broad absorbances, which may be attributed MoS_2. As previously shown, modest MoS_2 exfoliation can be achieved in water. That said, comparison of the spectra achieved for the control with the two peptide-based systems clearly demonstrated enhanced nanosheet production in the presence of both CMoSBP1 and MoSBP1. To compare the exfoliation efficiency, the absorbance intensity at 348 nm was compared between the three samples (Figure B4.1b). This wavelength was chosen because, at this point, there is a consistent minimum that is not affected by the varying layers of MoS_2. Other points in the spectra may shift due to defects in the sheets, conformational differences, or sheet thickness; thus, observing the absorbance at 348 nm provides a uniform measurement for quantifying concentration. From this comparison, the control reaction intensity was substantially lower than for the reactions with the peptides, indicating negligible MoS_2 nanosheet exfoliation. For the peptide-driven systems, a slight increase in the absorbance for the MoSBP1-exfoliated system was observed over the CMoSBP1-based reaction, suggesting enhanced MoS_2 sheet production from the uncapped peptide. However, the MoSBP1 peptide was substantially more soluble in water, as compared to CMoSBP1, which may affect the exfoliation efficiency.

The success of this exfoliation process requires successful outcomes for two stages: first, the sheets must be able to be detached from the bulk material during sonication, and second, these detached sheets must be prevented from re-associating once the sonication process is completed. Although experiments can evaluate the success of exfoliation via observation of the resultant colloidal suspension, it is challenging for experiment to directly verify the specific details of these two stages; however, MD simulations can provide atomic-scale insights into each stage of this process. The MD simulation data indicate that bare 2D nanosheets (*i.e.*, in the absence of peptide) of MoS_2 that were physically exfoliated by sonication were unlikely to maintain long-term colloidal stability in liquid water. In these simulations, a stack of 10 MoS_2 sheets of dimension ~5x5 nm in liquid water was modeled with an expanded inter-sheet gap between the top sheet and the remainder of the stack, to mimic gap expansion during sonication. This is depicted in Figure B4.2 (but in this case, without any peptide present). In the absence of peptide, the gap collapse started after an average of 7.4 ns of simulation, and it completely closed after 9 ns of simulation. The mechanism of gap collapse took place in two steps. In the initial step, the top sheet of MoS_2 started to be attracted to the bottom stack and moved downward the stack half gap distance (~5 Å), corresponding to expulsion of one layer of water inside the gap. This first stage took a total ~100 ps. Thereafter, the second water layer was expelled in the next ~1.4 ns. In total, after ~9 ns the expanded gap was completely closed. This result indicates that individual 2D nanosheets of MoS_2 will rapidly re-unite with the MoS_2 stack in pure water. All simulated mechanism data agree with the experimental results of the control sample and can explain why MoS_2 cannot be sufficiently exfoliated via sonication in liquid water alone.

Next, MD simulations were used to explore if the expanded gap could remain open for a longer period than that observed for the no-peptides scenario. This was tested with two types of simulation on the MoS_2 stack: pre-inserted simulations and spontaneous insertion simulations. The former was used to evaluate the maintenance of this expanded gap as a function of time in the presence of pre-inserted peptides (placed inside the expanded gap prior to commencing the simulations), compared with the stability of the gap in the absence of peptides. Similarly, the latter were also conducted to evaluate gap stability via the spontaneous ingress of peptides from solution into this expanded gap. With the presence of MoSBP1 peptide chains in the solvent, spontaneous insertion of these biomolecules into the expanded gap was observed almost immediately (within 2.2 ns for the vertical initial arrangement, Figure B4.2). For the parallel initial arrangement (in which the

peptide chains were placed parallel with the sheet plane, nearby to the gap), the spontaneous insertion took only ~1.3 ns, which is two times shorter than for the vertical initial arrangement of MoSBP1 peptides. The longer time seen for the initial vertical arrangement is understandable due to steric challenges of the ingress of the vertically arranged peptides. As a result, the gap was maintained during the simulation (20 ns) following the spontaneous insertion of the peptides, although at the end of simulation not all chains had entered the gap (Figure B4.2). Note that for the capped peptide (CMoSBP1), spontaneous peptide insertion also occurred, again for the duration of the 20 ns simulation. These simulation results are consistent with the experimental exfoliation efficiency data represented by the UV-vis data presented in Figure B4.1 where both capped and uncapped peptides were able to exfoliate bulk MoS_2. As a result, the gap was maintained during the simulation (20 ns) following the spontaneous insertion of the peptides, although at the end of simulation not all chains had entered the gap (Figure B4.2). Note that for the capped peptide (CMoSBP1), spontaneous peptide insertion also occurred, again for the duration of the 20 ns simulation. These simulation results are consistent with the experimental exfoliation efficiency data represented by the UV-vis data presented in Figure B4.1 where both capped and uncapped peptides were able to exfoliate bulk MoS_2.

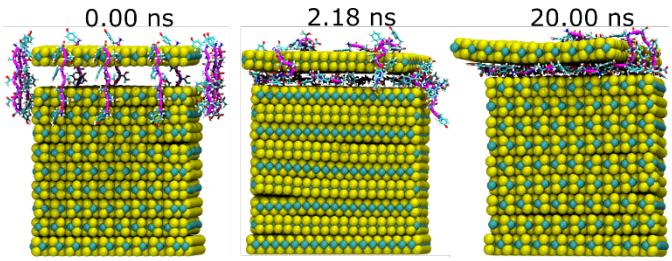

Fig. B4.2. Snapshots of spontaneous insertion of MoSBP1 peptides into the expanded gap. The initial arrangement of MoSBP1 is vertical to the MoS_2 nanosheet plane. Simulation-averaged insertion time shown. Water molecules not shown for clarity.

To experimentally confirm the interaction between the peptide and MoS_2, FT-IR was employed. Figure B4.1c presents the FT-IR spectra of an aqueous solution (MoSBP1 – red spectrum), bulk MoS_2 (black spectrum), and the MoSBP1-exfoliated MoS_2 nanosheets (blue spectrum). For the bulk MoS_2 powder, no significant stretching bands were observed over the wavelengths of interest, as anticipated. Conversely, the MoSBP1 peptide solution displayed a peak at ~3350 cm^{-1} for the symmetrical stretching of the N-H vibrations, as well as a peak at 3280 cm^{-1} for the antisymmetric stretching. The peak at 1590 cm^{-1} arises from the N-H bending, while the other peak at around 1650 cm^{-1} is for the C=O stretching, both arising from the amide backbone of the biomolecule. When examining the peptide-capped MoS_2 exfoliated sheets, the peaks for the peptide generally remained in the sample; however, their intensities were diminished, except for the N-H bending peak at 1590 cm^{-1}. This suggests that the peptides were indeed adsorbed to the nanosheet surface to facilitate exfoliation and colloidal stabilization in water. Zeta potential analysis of the exfoliated sheets was also conducted which gave rise to a surface charge of -32 and -35 mV for MoSBP1- and CMoSBP1-capped materials, respectively. The control exhibited a much lower charge at around -20 mV. Dynamic Light Scattering (DLS) was attempted; however, due to peptide aggregation, the measurements were inconclusive.

To confirm the structures of the isolated materials, the peptide-assisted exfoliated sheets were imaged using HRTEM, as presented in Figure B4.3. The interplanar spacing for MoSBP1 exfoliated sheets was found to be 0.255 nm. The darker contrasted areas in Figures B4.3a and b, are multiple sheets layered over one another. Figure B4.3b gives a more in-depth image of possibly two MoS_2 sheets on top of one another and shows overlaid crystalline structures of multiple sheets were observed. The TEM with CMoSBP1 exfoliated sheets showed multiple layers of MoS_2, as seen with Figure B4.3c; there are specific areas that show distinct structures of between 3-4 layers.

The same can be seen in Figure B4.3d, where there is a single long structure that has 4 distinct layers. This suggests that the CMoSBP1 may not exfoliate the materials with the same level of efficiency as the uncapped peptide.

As observed from the UV-vis and TEM analyses, the exfoliation processes with the capped peptide, CMoSBP1, had less exfoliation efficiency. In addition, the exfoliated nanosheets tended to form thicker structures consisting of 3 to 4 MoS_2 layers (Figure B4.3d) in comparison to those obtained from the exfoliation processes assisted with the uncapped peptide MoSBP1. To investigate this further, umbrella sampling MD simulations were performed to estimate the free energy of interaction of MoS_2 nanosheets, decorated with capped and uncapped peptide chains. The potential of mean force (PMF) profiles for the unification of two peptide-decorated MoS_2 sheets in liquid water are given for each case in Figure B4.4. In these simulations, two identical peptide-decorated (either CMoSBP1 or MoSBP1) MoS_2 sheets (34 peptides per sheet, 17 per side) that were initially arranged face-to-face (perpendicular to the sheet plane), where the distance between centers of the two sheets was 5 nm. The system was solvated in liquid water. A total of 55 configurations were used in the umbrella sampling simulations, for which the two sheets were drawn closer together and the reaction coordinate for the free energy profile was defined by the vertical inter-sheet distance. Each umbrella sampling window was simulated for 100 ns. The resultant free energy profile describing the approach of the two peptide-decorated sheets can indicate the general stability of the suspension.

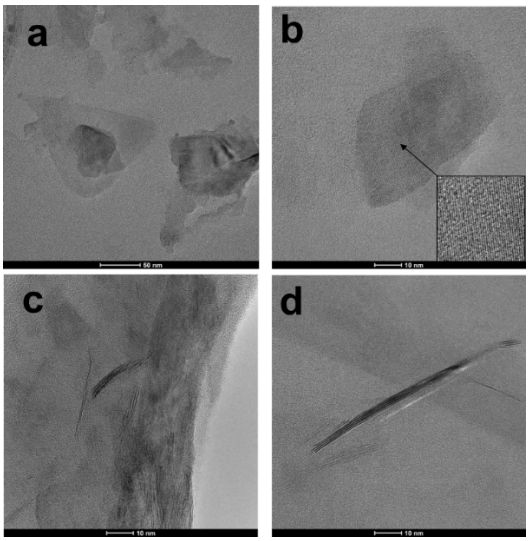

Fig. B4.3. TEM images of the MoS_2 materials exfoliated with (a and b) MoSBP1 and (c and d) CMoSBP1.

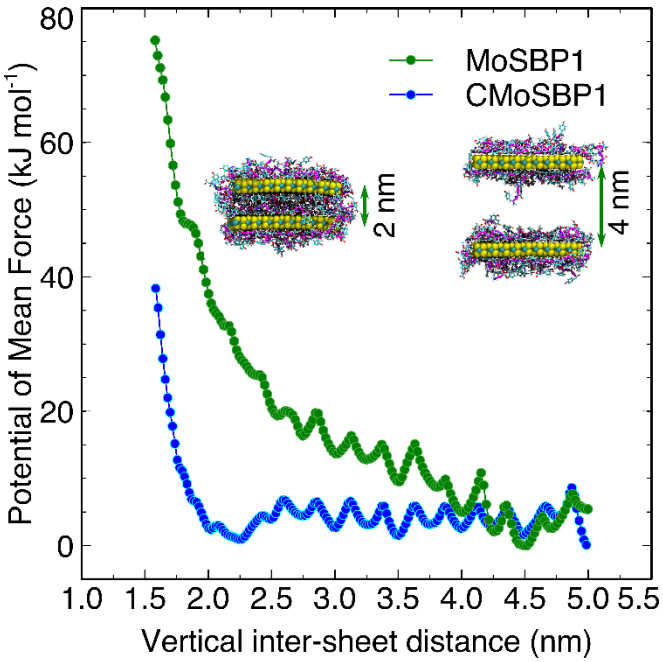

Fig. B4.4. PMF associated with the reunification of two MoS_2 nanosheets decorated with capped CMoSBP1 (blue) and uncapped MoSBP1 (green) peptides. The vertical inter-sheet distance is the distance between the two centers of mass of the MoS_2 nanosheets, excluding all attached peptides.

The PMF profiles from the two umbrella sampling simulations for MoS_2 nanosheets decorated with capped and uncapped peptides can give insights into the resultant colloidal stability following exfoliation. Two key interaction behaviors can be observed from these two PMF profiles. The first can be seen through the magnitude of repulsive forces once the two peptide-decorated sheets approach each other. Two MoS_2 nanosheets decorated with uncapped peptides MoSBP1 repulse each other with approximately double the strength compared with nanosheets decorated with the capped version

of peptides CMoSBP1 when the two nanosheets were close to each other (at an inter-sheet distance of ~1.5 nm). A second distinction between the capped and uncapped systems was found in the repulsive inter-sheet region between two MoS_2 nanosheets. The MoS_2 nanosheets with uncapped MoSBP1 peptides started to repulse each other at an inter-sheet distance of ~4.0 nm. Once the inter-sheet distance reduced to ~2.5 nm, the repulsive force started to exponentially increase and reaches ~80 kJ mol^{-1} at 1.5 nm. On the other hand, MoS_2 nanosheets decorated with capped peptides are not as repelled for inter-sheet distances from 2.2 to 4.0 nm; the repulsion was observed for inter-sheet distances of less than ~2.2 nm. Both a greater repulsive force and longer-distance repulsion observed in MoS_2 nanosheets decorated with uncapped MoSBP1 peptides indicate that these decorated sheets are inhibited from reunification, whereas those covered with the capped peptides CMoSBP1 may approach each other as close as a distance of ~2.2 nm. Such a close approach can allow more opportunities for aggregation if peptides are slightly detached from the decorated sheets. The PMF profiles are consistent with the experimental outcomes, specifically that CMoSBP1 confers less efficiency in the exfoliation of MoS_2 stacks, and that exfoliated MoS_2 nanosheets in the capped peptide system yield multiple layers of MoS_2 (up to 4 layers, Figure B4.3d).

Analysis of water inside the gap between the two approaching sheets revealed that MoS_2 nanosheets decorated with uncapped peptides MoSBP1 were more hydrated in comparison to those decorated with capped version of peptides (data not shown). At the closest intersheet distance of ~1.52 nm, the nanosheets with uncapped peptides have ~20% more water molecules in the space between the MoS_2 nanosheets than those decorated with capped peptides (509 vs 427 water molecules). This result is understandable because the uncapped peptides have charged termini (NH_3^+ and COO^-), while the termini of CMoSBP1 chains are capped with the hydrophobic CH_3 groups. As a result, the MoS_2 nanosheets exfoliated with MoSBP1 peptides are better solvated, and it is possible this additional solvation contributes to the enhanced colloidal stability in the uncapped case.

The umbrella sampling simulations suggest that uncapped MoSBP1 peptides can make contact with their counterpart attached to the opposite MoS_2 sheets at a longer distance of inter-sheet gaps. At the inter-sheet distance of ~3.10 nm, the uncapped peptide chains can make contact with their counterparts on the opposite MoS_2 nanosheet, whereas in the capped CMoSBP1 system, the surface-adsorbed chains on the two sheets remain distant (data not shown). Quantitatively, at the inter-sheet distance of ~3.1 nm, the mass density of uncapped MoSBP1 peptides at the mid-point of the gap between the two MoS_2 nanosheets is ~5.0 kg m^{-3}, while this value of capped CMoSBP1 ones is ~0 kg m^{-3} (red line in the green dashed circle, Figure B4.5a). The capped CMoSBP1 peptides started to make contact at a shorter gap distance (~2.45 nm). This can be seen through the non-zero mass density (~5.0 kg m^{-3}) of capped peptides at this mid-point

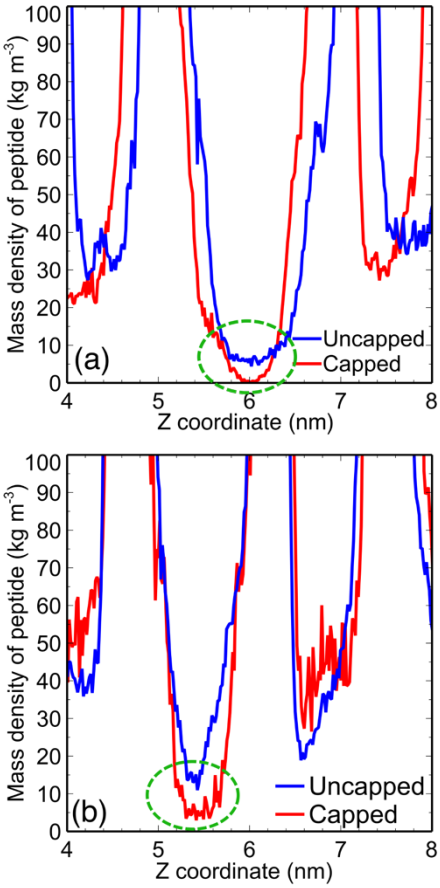

Fig. B4.5. Mass density of peptides perpendicular to the sheet plane measured at the inter-sheet gap distances of (a) 3.10 nm and (b) 2.45 nm. The densities in the middle regions are circled in green dashed lines.

shown in Figure B4.5b (red line in the green dashed circle), while the mass density of uncapped peptides (blue) is ~15 kg m^{-3}, which is three times higher than that of the capped peptides. In general, for the same intersheet separation, uncapped peptides were more present at the mid-point region, and hence could better protect MoS_2 nanosheets from aggregation. The onset of this protection also can happen at greater inter-sheet vertical separations (3.10 nm *vs.* 2.45 nm). Together with stronger solvation discussed above, protection from aggregation at greater inter-sheet vertical separations along with the higher density of uncapped peptides at the intersheet spacing midpoint can support more stable MoS_2 nanosheets decorated with uncapped MoSBP1 chains.

Analysis of residue contact time can reveal how individual residues of peptides remain in contact with the MoS_2 nanosheets. The data obtained at two gap distances of 3.10 and 2.45 nm (data not shown) show that the charged groups NH_3^+ of the uncapped peptides spend more time, on average, in the solution (~70% of time) while the neutral groups of the acylated capped CMoSBP1 spend more time in contact with the MoS_2 sheets (60% of time). In contrast, the two terminal groups COO^- and the capping NME (N-methyl amide) group of the uncapped and capped peptides, respectively, were in contact with the MoS_2 surface ~40% of time. From the distribution of strongest-contact residues (at the intersheet separations of 3.10 and 2.45 nm) with > 80% contact time, on the upper sheet the number of strongest-contact residues in the capped CMoSBP1 peptides is higher than those in the uncapped MoSBP1 system (at 3.10 nm: 3 and 0; at 2.45 nm: 3 and 0, respectively). On the lower sheet, at the intersheet distance of 3.10 nm, a sole residue (Tyr1) in the uncapped system and the residue Tyr7 in the capped system were found to be the strongest-contact residues, but the acylated terminal group of the capped peptides had 71% contact time, resulting in both ends of the capped peptides most likely touching the MoS_2 surface much of the time. A similar situation can be observed in the lower sheet at the intersheet distance of 2.45 nm for the capped peptides, where the terminal acyl group (52% contact time) and the strongest-contact residue (Phe5) were in contact most of the time, while the uncapped peptides tended to have more freedom at one end (from residues Thr4 to Tyr7). Note that in this case, the Tyr7 residue of the capped peptides also has a high contact time (79%) and is proposed to contribute to intensive contact of the capped peptides to the MoS_2 surface as well. The lesser average contact time of the uncapped peptide residues and terminal groups, to an extent, is proposed to explain why uncapped peptides can make contact with peptides on the opposite MoS_2 nanosheet at a greater intersheet separation, resulting in higher mass density in the midpoint region of the inter-sheet spacing.

With confirmation of the stability of the exfoliated materials, the thickness of the MoSBP1-exfoliated MoS_2 sheets was further examined via AFM, as shown in Figure B4.6. Since the TEM data indicated that the CMoSBP1 peptides were not as efficient at MoS_2 exfoliation, additional AFM analysis was not conducted on these materials. Figure B4.6a specifically presents the AFM image of the MoSBP1-exfoliated materials. Statistical analysis of >100 nanosheets was conducted (Figure B4.6b), demonstrating an average thickness of 2.6 ± 1.1 nm for this sample. Such a value indicates MoS_2 sheets ranging from 2 to 4 layers present in the sample. Interestingly, a bimodal distribution was noted, suggesting a mixture of individual sheets and small stacks was present in the sample.

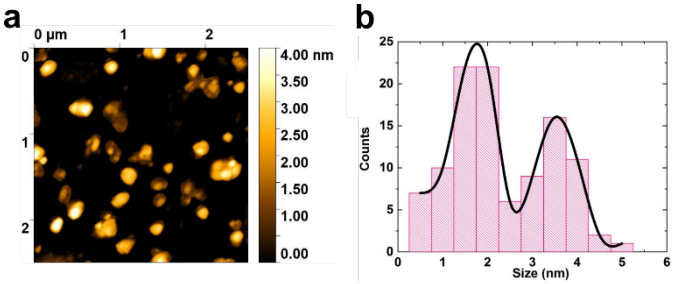

Fig. B4.6. AFM analysis of the MoS_2 materials exfoliated using MoSBP1. Part (a) presents the AFM image, while part (b) presents a statistical height analysis of the materials.

The Raman spectra of both peptide-driven MoS_2 exfoliations were measured at an excitation of 514.5 nm and were taken from multiple areas on the surface (Figure B4.7). For the MoSBP1 and CMoSBP1, the peaks located at ~380 cm^{-1} corresponded to the in plane opposing vibrations of the sulfur and molybdenum atoms (phonon mode E^1_{2g}). The second peak located at ~400 cm^{-1} is indicative of the out of plane vibrations of the sulfur atoms that are on either side of the molybdenum (phonon mode A1g). The few layers of MoS_2 would cause a blue shift in both peaks due to the increased energy from scattered photons from the material. The absence of E_{1g}, J_1, J_2, and J_3 peaks in the spectra supports the formation of the 2H MoS_2 nanosheets rather than the 1T form that these peaks would represent.

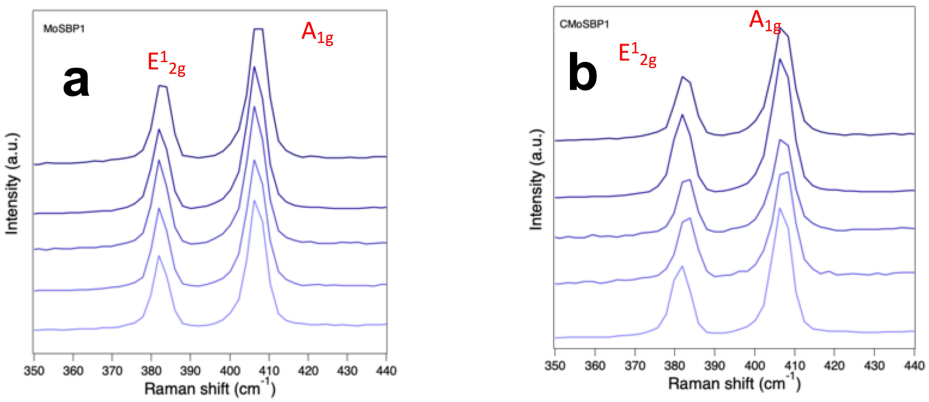

Fig. B4.7. Raman analysis of the MoS_2 nanosheets exfoliated with (a) MoSPB1 and (b) CMoSBP1.

Finally, XPS analysis of the MoSBP1-exfoliated MoS_2 materials was performed, which confirmed the generation of the peptide-capped materials. Figure B4.8a demonstrates the presents of Mo^{4+}, with a deconvoluted 3*p* peak at 398 nm, and evidence of nitrogen from the peptide at 400.5 nm (1*s* peak). Note that the peak associated with nitrogen is quite low in intensity due to its low concentration with respect to Mo in the sample. At 230 and 233 eV, the binding energy of the 3*d* orbital for Mo^{4+} in 2H MoS_2 was also observed, arising from the $3d_{3/2}$ and $3d_{5/2}$, respectively (Figure B4.8b). Additionally, the peak at 227 eV originates from the 2*s* orbital of the sulfur atoms of MoS_2. Furthermore, Figure B4.8c displays the peaks for the $2p_{1/2}$ (161 nm) and $2p_{3/2}$ (160 nm) spin orbitals of sulfur. Interestingly, an unexpected peak was observed at 167 eV, which likely arises from oxidation of the sulfur atoms in MoS_2 to a sulfoxide. Previous studies of MoS_2 exfoliation have demonstrated such oxidation can occur to generate either SO_3 or SO_4.

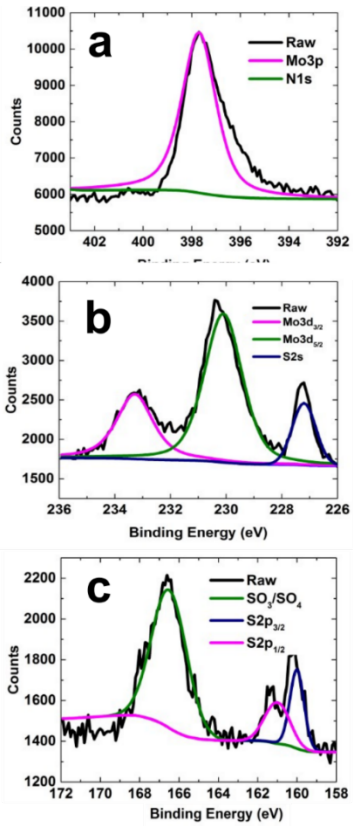

Fig. B4.8. XPS analysis of the MoSBP1-exfoliated MoS_2 materials.

In conclusion, MoS_2 materials have been exfoliated in aqueous media with the support of a MoS_2-binding peptide and sonication. Both capped CMoSBP1 and uncapped MoSBP1 peptides were demonstrated to facilitate the exfoliation process, in which uncapped MoSBP1 peptides were found to be more efficient in exfoliating the MoS_2 into smaller structures. The exfoliated nanosheets were found to have different morphologies based upon the capped *vs*. uncapped structure of the peptide, which likely arises from the interactions between the material and biomolecule. Molecular simulations of both the initial exfoliation process and the stability of the resultant exfoliated sheets in solution were both consistent with the

experimental data. Specifically, the simulations suggest that the presence of the peptides is critical for enabling the first step of the exfoliation mechanism by maintaining the expanded gap induced by sonication. Furthermore, the experimentally observed differences in the exfoliated product for the capped and uncapped systems can in part be explained by the free energy profiles related to the reunification of peptide-decorated MoS_2 nanosheets. The lesser protection conferred by the capped peptides is likely due to the fact that the sheets decorated by capped peptides can approach relatively closer compared with their uncapped counterparts. These findings provide a bio-based platform for the manipulation, organization, and activation of MoS_2 materials in aqueous media. Such effects could prove to be highly important in the design of new nanoscale systems and devices that require surface conjugation on the MoS_2 materials without covalent attachment or defect incorporation.